International Journal of Mechanical Sciences 70 (2013) 1–25

Contents lists available at SciVerse ScienceDirect

International Journal of Mechanical Sciences

journal homepage: www.elsevier.com/locate/ijmecsci

Three-dimensional vibrations of cracked rectangular parallelepipeds of functionally graded material

C.S. Huang [a], O.G. McGee III[b,*], K.P. Wang [a]

[a] Department of Civil Engineering, National Chiao Tung University, 1001 Ta-Hsueh Rd., Hsinchu, Taiwan 30050, Republic of China (R.O.C.)
[b] Department of Mechanical Engineering Howard University Washington DC, U.S.A.

ARTICLE INFO

Article history:
Received 12 July 2011
Received in revised form
11 May 2012
Accepted 15 May 2012
Available online 26 June 2012

Keywords:
Vibrations
Cracked rectangular parallelepiped
Ritz method
3-D elasticity
Functionally graded material (FGM)

ABSTRACT

A novel examination of the three-dimensional (3-D) vibrations of rectangular parallelepipeds of functionally graded material (FGM) having side cracks is summarized. Employing 3-D theory of elasticity and a variational Ritz methodology, new hybrid series of mathematically complete orthogonal polynomials and crack functions as the assumed displacement fields are proposed to enhance the convergence modeling of the stress singular behavior of the crack terminus edge front in a rectangular FGM parallelepiped. The proposed admissible hybrid series properly describe the $\vartheta(1/\sqrt{r})$3-D stress singularities at the terminus edge front of the crack, allowing for displacement discontinuities across the crack sufficient to explain the most general 3-D "mixed modes" of local crack-edge deformation and stress fields typically seen in fracture mechanics. The correctness and validity of the vibration analysis are confirmed through comprehensive convergence studies and comparisons with published results for cracked rectangular FGM parallelepipeds modeled as homogeneous rectangular plates with side cracks and FGM rectangular plates with no cracks based on various plate theories. Two types of FGM parallelepipeds, Al/Al_2O_3 and Al/ZrO_2, are included in the study. The locally effective material properties are estimated by a simple power law and the effects of the volume fraction on the frequencies are investigated. For the first time in the published literature, this work reports frequency data and nodal patterns for FGM rectangular parallelepipeds modeled as moderately thick plates with several combinations of hinged, clamped, and completely free kinematic and stress conditions along the four side faces, and having side cracks with varying crack size effects implying flaw-size influence in FGM parallelepiped vibration and fracture, including crack length ratios (d/a and d/b), crack positions (c_x/a and c_y/b), and crack inclination angles (α).

© 2012 Elsevier Ltd. All rights reserved.

1. Introduction

Laminated composite materials are prevalent in engineering systems, particularly in aeronautical vehicles and aerospace structures. However, the abrupt change in material properties across the interface between material layers can cause large inter-laminar stresses even some de-laminations. Functionally graded materials (FGMs) [1] are found to overcome these adverse interlamination stress and delamination effects associated with conventional laminated composite builds. Material properties of FGMs vary continuously by gradually changing the volume fraction of constituent material properties. FGMs have been extensively explored in the last two decades along a variety of interdisciplinary fronts, including electronics, chemistry, optics, biomedicine, aeronautical and mechanical engineering.

Rectangular parallelepipeds modeled as plates are employed in a wide range of mechanical and structural system components in civil, mechanical and aeronautical engineering. Such rectangular parallelepipeds are oftentimes subjected to irregular loads generated by waves or subjected to cyclic loads induced by machinery. Consequently, fatigue cracks may be initiated in the parallelepiped components. Vibrations of fractured FGM parallelepipeds require dynamic stress analysis of their sensitivity to flaws or crack-liked defects with high local stresses progressing through crack propagation mechanisms lengthening even inclining fatigue cracking.

Redistribution of stresses in cracked FGM parallelepipeds causes dynamic characteristics markedly different from those for an intact parallelepiped, requiring linear-elastic stress analysis, including elevated stresses local to the crack terminus edge. Here, the free surfaces of the crack dynamically moving relative to each other significantly influence the distribution of

* Corresponding author. Tel.: +1 614 404 5427.
E-mail addresses: cshuang@mail.nctu.edu.tw (C.S. Huang), ogmcgee@yahoo.com (O.G. McGee III).

0020-7403/$ - see front matter © 2012 Elsevier Ltd. All rights reserved.
http://dx.doi.org/10.1016/j.ijmecsci.2012.05.009

stresses local to the crack terminus edge. Various combinations of clamped, free, and hinged boundary conditions of a cracked parallelepiped affect the intensity of the local dynamic stress field at the crack terminus edge. The dynamic stress field near the crack terminus edge within a FGM parallelepiped may be classified as three basic dynamic responses each associated with a local mode of crack deformation. First, a crack opening mode in FGM parallelepiped vibration is associated with local displacement in which the crack surfaces move directly apart; second, a crack shearing or edge-sliding mode in FGM parallelepiped vibration is characterized by deformations in which the crack surfaces slide over one another perpendicular to the leading terminus edge of the crack; third, a crack tearing mode in FGM parallelepiped vibration finds the crack surfaces sliding with respect to one another parallel to the leading terminus edge of the crack. Crack opening and crack shearing or edge-sliding in FGM parallelepiped vibration can be modeled as two-dimensional plane-extension theory of elasticity, classified as symmetric (crack opening) and skew-symmetry (crack shearing/sliding) with respect to the leading edge of the crack. Crack tearing in FGM parallelepiped vibration may be modeled as two-dimensional pure shear (or torsion). Well-known superposition of crack opening, shearing or sliding, and tearing modes or "mixed mode" cracking in FGM parallelepiped vibration is sufficient to describe the most general three-dimensional dynamic aspects of local crack-edge deformation and stress fields in cracked parallelepipeds. Such local crack-edge deformation and stress fields involve trigonometric distributions in a circumferential coordinate (θ) ($x=\cos\theta$, $y=\sin\theta$, see Fig. 1) local to the crack terminus edge. The crack-edge stress fields are dominated by the order of an inverse square root of a local polar coordinate ($r=\sqrt{x^2+y^2}$, see Fig. 1), $\vartheta(1/\sqrt{r})$, emanating from the crack terminus edge, whereas the crack-edge deformations are dominated by the order of a square root of the local polar coordinate, r, $\vartheta(1/\sqrt{r})$.

Hence, a need arises to establish these linear-elastic crack-edge stress (and displacement) fields in the dynamic characteristics of cracked parallelepipeds, specifically modeled herein as cracked thick plates to provide reference three-dimensional (3-D) solutions that delineate validity and accuracy of a growing database of cracked plates in the literature recently offered by Huang and co-workers using classical Kirchhoff thin-plate theory [2,3], proposed by Li [4] using first-order shear deformable Mindlin plate theory, and reported by Huang and Chang using [5] higher third-order shear deformable plate theory.

Lynn and Kumbasar [6], Stahl and Keer [7], Aggarwala and Ariel [8], Neku [9], Solecki [10], Hirano and Okazaki [11], Qian et al. [12], Krawczuk [13], Yuan and Dickinson [14], Liew et al. [15], and Huang and Leissa [2,3] proposed various approximate solution techniques using classical Kirchhoff thin-plate theory to study the vibrations of cracked rectangular parallelepipeds, modeled as homogeneous thin plates. Lee and Lim [16] employed a simplified Reissner theory and the Ritz method along with a subdomain technique to examine the vibrations of cracked rectangular parallelepipeds modeled as thick plates including transverse shear deformation and rotary inertia. Maruyama and Ichinomiya [17], Ma and Hsieh [18], and Ma and Huang [19] established an experimental bench test database of cracked thin homogeneous plates.

Documented in the published literature are substantial findings on vibrations of parallelepipeds modeled as thick homogeneous plates and FGM plates with no cracks. Yang and Shen [20] and He et al. [21] used the classical plate theory, while Zhao et al. [22] and Reddy [23] adopted the first-order and the third-order shear deformation plate theories, to investigate vibrations of FGM plates with no crack. Matsunaga [24] and Qian et al. [25] proposed solutions for vibrations and stability of FGM rectangular shear deformable plates incorporating higher-order transverse shear effects. Vel and Batra [26] proposed a three-dimensional exact vibration solution of simply-supported thick FGM plates and Reddy and Cheng [27] presented a three-dimensional asymptotic solution for vibrations of simply-supported FGM plates.

However, there appears to be no published findings of accurate vibration frequencies and nodal patterns for arbitrarily-oriented and positioned cracked FGM parallelepipeds having various combinations hinged, clamped or simply-supported face conditions. In the above-mentioned literature, the solutions, except for

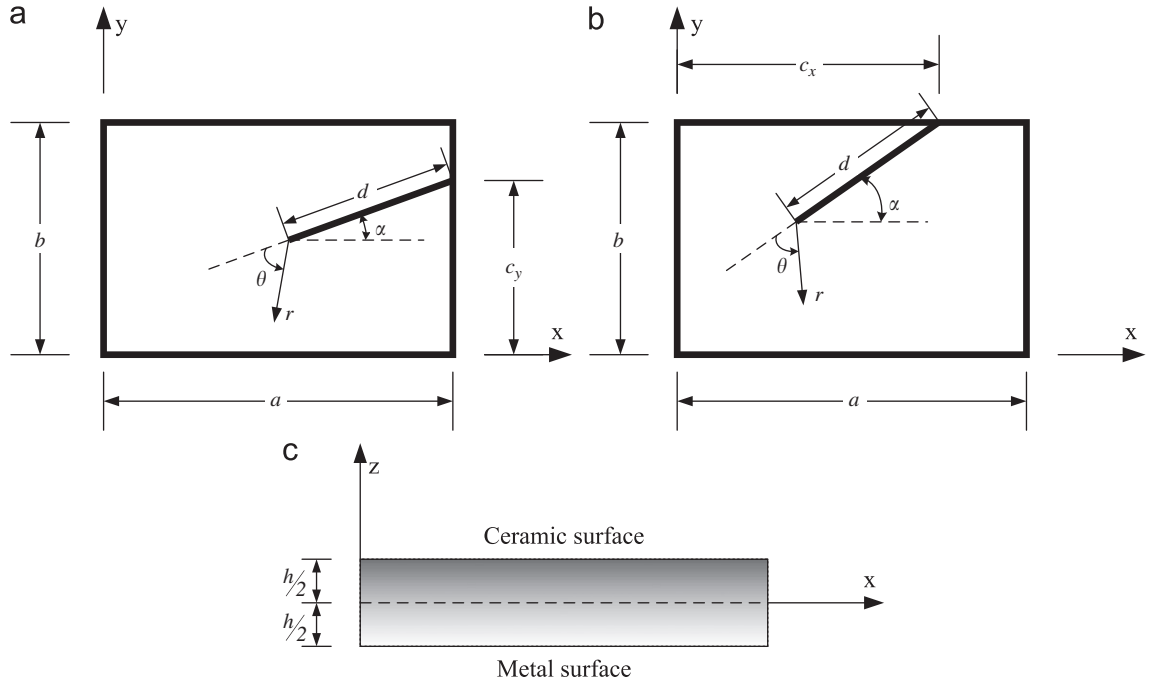

Fig. 1. A rectangular Functionally Graded Material (FGM) parallelepiped modeled as a thick plate having a side crack showing position coordinates (c_x and c_y), crack length (d), and crack orientation (α); (a) top view of a plate with a crack intersecting $x=$a; (b) top view of aplate with a crack intersecting $y=$b and (c) side view of plate.

the finite element solutions, by no means considered the characteristic of the stress singularities at the crack terminus edge. The present work proposes a novel 3-D elasticity-based Ritz variational procedure to investigate the vibrations of side-cracked rectangular parallelepipeds modeled as thin and thick plates. The novelty of the analysis incorporates into the displacement fields of the dynamical energies, a hybrid series of mathematically complete admissible orthogonal polynomials [28] and newly-developed *crack functions* accounting for stress singularities at the front of the crack and allowing for displacement discontinuities across the crack (sufficient to describe the most general 3-D mixed modes of local crack-edge deformation and stress fields), altogether accurately predicting the vibrations of FGM parallelepipeds with side cracks.

Based on 3-D elasticity theory, Hartranft and Sih [29], Chaudhuri and Xie [30], Williams [31], and Erdogan and Sih [32] established eigenfunction expansions showing stress singularities in statically-loaded cracked homogenous parallelepipeds. The most direct approach in determining the stress and displacement fields associated with each crack-edge mode draws upon fundamentals of fracture put forth early-on by Irwin [33] using methodologies originally proposed by Westergaard [34]. Recently, the free vibrations of cracked FGM parallelepipeds modeled as Kirchhoff thin plates [35] and higher-order Reddy shear deformable thick plates [36] have been addressed.

The present 3-D Ritz methodology is validated by comprehensive convergence studies and by comparisons of published solutions obtained using alternative theories and methods for cracked homogeneous and FGM parallelepipeds modeled as thin [35] and shear deformable thick plates [36]. An extensive amount of non-dimensional frequencies and nodal patterns are reported herein for the first time for FGM rectangular parallelepipeds modeled as moderately thick plates having various combinations hinged, clamped or simply-supported face conditions, and having side cracks with different crack length ratios (d/a and d/b), crack positions (c_x/a and c_y/b), and crack inclination angles (α). The effects of the volume fraction in a power law for describing material properties of FGM on the frequencies are also examined. These results can serve as the benchmark values for future numerical techniques in plate vibrations and for establishing simplified FGM plate theories and asymptotic perturbation solutions.

2. Theoretical formulation

Consider in Fig. 1 the rectangular coordinates (x,y,z) assumed originating at the mid-plane of a rectangular FGM parallelepiped modeled as a thick plate with a side crack. Seen also therein are the polar coordinates (r,θ) assumed emanating at the tip of crack on the mid-plane, which are used to describe in the limit as r approaches zero the infinite stress at the crack front.

The material properties (*i.e.*, elastic modulus, $E=E(z)$, Poisson's ratio, $\upsilon=\upsilon(z)$ and mass density, $\rho=\rho(z)$) vary as a simple power law in the parallelepiped thickness (*i.e.*, the z direction in Fig. 1), as follows:

$$P(z)=P_b+V(z)\Delta P \tag{1}$$

where $V(z)=\left(\frac{z}{h}+\frac{1}{2}\right)^{\hat{m}}$, P_b denotes the properties at the bottom parallelepiped face $z=-h/2$ ΔP, is the difference between P_b and the corresponding property at the top parallelepiped face ($z=h/2$); h is the parallelepiped thickness, and $\hat{m}$ is the parameter of volume fraction that governs the material variation profile in the thickness direction. In the present study, the FGM parallelepipeds under consideration are made of aluminum (Al) and ceramic (zirconia (ZrO_2) or alumina (Al_2O_3)), whose material properties are given in Table 1.

Table 1
Material properties of the FGM components.

Material	Properties		
	E (GPa)	Poisson's ratio (ν)	ρ (kg/m^3)
Aluminum (Al)	70	0.3	2702
Alumina (Al_2O_3)	380	0.3	3800
Zirconia (ZrO_2)	200	0.3	5700

In using the Ritz method, the dynamic characteristics of the parallelepiped are predicted by minimizing the energy functional

$$\Pi=V_{\max}-T_{\max}, \tag{2}$$

where $V_{\max}$ is the maximum strain energy and $T_{\max}$ is the maximum kinetic energy in simple harmonic motion, $e^{\sqrt{-1}\omega t}\rightarrow 1$. Based on 3-D elasticity theory, a parallelepiped vibrating harmonically with circular frequency ω and amplitudes U_i (x, y, z) ($i=1,2,3$) along the x, y and z coordinate directions, respectively, is described by the following maximum strain and kinetic energy expressions at the peak displacements and velocities of the vibratory cycle:

$$V_{\max}=\frac{1}{2}\int_V\Big\{\lambda(z)(U_{1,x}+U_{2,y}+U_{3,z})^2+G(z)\Big[2(U_{1,x})^2+2(U_{2,y})^2 +(U_{2,z}+U_{3,y})^2+(U_{3,x}+U_{1,z})^2\Big]\Big\}dV, \tag{3a}$$

$$T_{\max}=\frac{\omega^2}{2}\int_V\rho(z)(U_1^2+U_2^2+U_3^2)dV, \tag{3b}$$

where $\lambda(z)=\frac{\upsilon(z)E(z)}{(1+\upsilon(z))(1-2\upsilon(z))}$ and $G(z)=\frac{E(z)}{[2(1+\upsilon(z))]}$, with the subscript comma in Eq. (3) denoting partial differentiation with respect to the coordinate defined by the variable after the comma.

Displacement amplitude functions, U_i (x,y,z), are expressed in terms of admissible functions, $\tilde{U}_{ij}(x,y,z)$, as

$$U_i(x,y,z)=\sum_{j=1}^{Ni}a_{ij}\tilde{U}_{ij}(x,y,z)\quad(i=1,2,3), \tag{4}$$

wherein the $\tilde{U}_{ij}(x,y,z)$, which is formulated shortly, are constructed in mathematical completeness to satisfy minimally the geometric (kinematical) conditions corresponding to the various combinations of hinged, clamped, and completely free face conditions of the cracked parallelepiped and additionally, the stress singularities at the front of the crack and displacement discontinuities across the crack. Substituting Eq. (4) into Eqs. (2) and (3) and minimizing the energy functional (Eq. (2)) with respect to the generalized coefficients, a_{ij}, (Eq. (4)), yields the following matrix set of linear homogeneous algebraic equations:

$$\begin{bmatrix}\mathbf{K}^{11} & \mathbf{K}^{12} & \mathbf{K}^{13}\\ & \mathbf{K}^{22} & \mathbf{K}^{23}\\ sym & & \mathbf{K}^{33}\end{bmatrix}\begin{Bmatrix}a_{1j}\\a_{2j}\\a_{3j}\end{Bmatrix}=\omega^2\begin{bmatrix}\mathbf{M}^{11} & \mathbf{M}^{12} & \mathbf{M}^{13}\\ & \mathbf{M}^{22} & \mathbf{M}^{23}\\ sym & & \mathbf{M}^{33}\end{bmatrix}\begin{Bmatrix}a_{1j}\\a_{2j}\\a_{3j}\end{Bmatrix}, \tag{5}$$

which is expressed in the form of a standard eigenvalue problem—the eigenvalues being the circular frequencies of free vibration ω of a cracked FGM parallelepiped. The associated eigenvectors of generalized coefficients, a_{ij}, may be substituted back into Eq. (4) to obtain the physical vibration mode shapes of the cracked FGM parallelepiped corresponding to each circular frequencies of vibration ω.

An appropriately enhanced Ritz procedure proposed herein yields accurate solutions of cracked FGM parallelepiped vibrations

with the accuracy and efficiency of the approximate solutions largely depending on the appropriate choice of $\tilde{U}_{ij}(x,y,z)$ in Eq. (4). A hybrid series of mathematically complete admissible orthogonal polynomials and newly-developed crack functions accounting for stress singularities at the front of the crack, while permitting displacement discontinuities across the crack, are used to approximate each of displacement amplitudes, U_i (x, y, z). In Eq. (4), the displacement amplitude functions are expressed as

$$U_i = \hat{U}_{ip} + \hat{U}_{ic} \tag{6}$$

where $\hat{U}_{ip}$ is an assumed finite series of mathematically complete polynomials; and $\hat{U}_{ic}$ is an assumed finite series of crack functions, supplementing the assumed polynomial series, $\hat{U}_{ip}$, to appropriately describe the essential singular stresses and displacement discontinuities across the crack.

Orthogonal polynomials are adopted to expand $\hat{U}_{ip}$in Eq. (6) as

$$\hat{U}_{ip}(x,y,z) = f_i(z)\sum_{l=1}^{N_{iz}}\sum_{j=1}^{N_{ix}}\sum_{k=1}^{N_{iy}} A_{jkl}^{(i)} P_j^{(i)}(x) Q_k^{(i)}(y) z^{l-1} \quad (i=1,2,3), \tag{7}$$

where $P_j^{(i)}(x)$and $Q_k^{(i)}(y)$ are orthogonal polynomials in the x and y directions, respectively, and are generated by using a standard Gram–Schmidt orthogonalization process [28]. Imbedded inside the adopted Gram–Schmidt orthogonalization procedure are associated boundary functions in which $P_j^{(i)}(x)$ satisfy the geometric boundary conditions for U_i on the parallelepiped faces, $x=0$ and $x=a$, while $Q_k^{(i)}(y)$ satisfy the geometric boundary conditions for U_i on the parallelepiped faces, $y=0$ and $y=b$. In Eq. (7), the assumed series of algebraic polynomials, z^{i-1}, resembles the kinematical assumption of displacements in the thickness (z) coordinate incorporated in various well-established Mindlin and higher-order shear deformable plate theories. Boundary functions, $f_i(z)$, are used to satisfy the geometric boundary conditions for U_i on the top and bottom parallelepiped faces. In this work, completely stress free top and bottom parallelepiped faces are assumed so that $f_i(z)=1$.

To enhance the convergence accuracy of the proposed Ritz procedure due to the presence of a crack, stress singularities at the front of the crack and displacement discontinuities across the crack are considered in constructing admissible crack functions, $\hat{U}_{ic}$, augmenting the assumed series of orthogonal polynomials, $\hat{U}_{ip}$. Based on 3-D elasticity theory, Hartranft and Sih [29] and Chaudhuri and Xie [30] established eigenfunction expansions showing a well-known stress singularity order of $-1/2$ for a cracked homogenous parallelepiped having completely free side cracks. Huang and Chang [35] and Huang et al. [36] further established that the vibrations of cracked FGM parallelepipeds modeled as Kirchhoff thin and Reddy shear deformable thick plates have analogous stress singularity order as a homogenous plate. Hence, the following set of crack functions is proposed for a cracked FGM parallelepiped:

$$\left\{ r^{(2n-1)/2}\cos\frac{2m+1}{2}\theta \text{ and } r^{(2n-1)/2}\sin\frac{2m+1}{2}\theta \;\middle|\; m=0,1,2,\ldots,n \text{ and } n=1,2,3,\ldots \right. \tag{8}$$

and $\hat{U}_{ic}$ in Eq. (6) is expressed as

$$\hat{U}_{ic}(r,\theta,z) = g_i(x,y,z)\sum_{l=1}^{N_{iz}}\sum_{n=1}^{\bar{N}_i}\sum_{m=0}^{n}\left[B_{nml}^{(i)} r^{(2n-1)/2}\cos\frac{2m+1}{2}\theta + C_{nml}^{(i)} r^{(2n-1)/2}\sin\frac{2m+1}{2}\theta\right] z^{l-1} \tag{9}$$

where $g_i(x,y,z)$ (i =1, 2, 3) are boundary functions to satisfy the geometric boundary conditions for U_i on the parallelepiped faces. The admissible functions in Eq. (9) yield the well-known fracture mechanics fact that (for $n=1$) the order of the 3-D stress tensor components are $\sigma_{ij}\sim\vartheta(1/\sqrt{r})$ as r approaches zero. Yet, the gradients of Eq. (9) are not continuous across a FGM crack ($\theta=\pm\pi$). Such displacement discontinuities across the crack are fully accounted for in establishing the admissibility of the crack functions through the boundary functions $g_i(x,y,z)$ (i=1, 2, 3). Note that the associated eigenvectors of generalized coefficients, a_{ij}, (Eqs. (4)–(5)) comprise the $A_{jkl}^{(i)}$ (from Eq. (7)), and $B_{nml}^{(i)}$ and $C_{nml}^{(i)}$ (from Eq. (9)).

Near the crack tip, where the terms corresponding to $n=1$ dominate, the assumed crack functions (Eq. (9)) possess a necessary positive square root in the polar coordinate r, (dominated by the order of square root of r, $\vartheta(\sqrt{r})$), and the associated 3-D stress fields possess the well-established square root singularity as r goes to zero (dominated by the order of inverse square root of r, $\vartheta(1/\sqrt{r})$, emanating from the crack-edge), thus, yielding the appropriate admissibility required regardless of the FGM parallelepiped geometry and normal mode response and stress distribution. By incorporating appropriate gradients of the displacement fields (Eqs. (7) and (9)), the associated 3-D stress fields of the cracked FGM parallelepiped are

$$\begin{aligned}
\sigma_x &= \lambda(z)(U_{1,x}) = \lambda(z)[\hat{U}_{1p,x} + \hat{U}_{1c,x}]\\
\sigma_y &= \lambda(z)(U_{2,y}) = \lambda(z)[\hat{U}_{2p,y} + \hat{U}_{2c,y}]\\
\sigma_z &= \lambda(z)(U_{3,z}) = \lambda(z)[\hat{U}_{3p,z} + \hat{U}_{3c,z}]\\
\tau_{xy} &= (G(z)/2)(U_{1,y} + U_{2,x}) = (G(z)/2)[(\hat{U}_{1p,y} + \hat{U}_{1c,y}) + (\hat{U}_{2p,x} + \hat{U}_{2c,x})]\\
\tau_{yz} &= (G(z)/2)(U_{2,z} + U_{3,y}) = (G(z)/2)[(\hat{U}_{2p,z} + \hat{U}_{2c,z}) + (\hat{U}_{3p,y} + \hat{U}_{3c,y})]\\
\tau_{xz} &= (G(z)/2)(U_{3,x} + U_{1,z}) = (G(z)/2)[(\hat{U}_{3p,x} + \hat{U}_{3c,x}) + (\hat{U}_{1p,z} + \hat{U}_{1c,z})]
\end{aligned} \tag{10}$$

wherein the above usual transformations between the global Cartesian (x,y,z) coordinates of the FGM parallelepiped and the local polar (r,θ,z) coordinates at the crack terminus edge are assumed in the present 3-D calculations.

Values of the generalized constants, $B_{nml}^{(i)}$ and $C_{nml}^{(i)}$, in Eqs. (9)–(10), depend on the cracked FGM parallelepiped geometry, boundary conditions, and the associated normal mode response; however, the polar coordinate dependence of the corner functions sequence (Eq. (8)) do not change with the cracked FGM parallelepiped geometry, boundary conditions, and normal mode response. Nonetheless, for n=1,2,3,…, the generalized constants, $B_{nml}^{(i)}$ and $C_{nml}^{(i)}$, in Eqs. (9)–(10), may be generalized as directly proportional to crack-edge stress (field) intensity factors [33,34] ($n=1$ being associated with the most dominant 3-D stresses in Eq. (10), see Appendix) through a proportionality constant $\sqrt{2\pi}$ for crack opening responses ($\sqrt{2\pi}B_{nml}^{(i)}$) and crack shearing or sliding responses ($\sqrt{2\pi}C_{nml}^{(i)}$), including more generalized 3-D "mixed-mode" crack opening-shearing/sliding-tearing responses (see Appendix), depending on the complexity of cracked FGM parallelepiped vibratory behavior. Given $\sqrt{2\pi}B_{nml}^{(i)}$ and $\sqrt{2\pi}C_{nml}^{(i)}$ are independent of r and θ, they embody the strength of the stress fields surrounding the crack edge. Alternatively, $\sqrt{2\pi}\,B_{nml}^{(i)}$ and $\sqrt{2\pi}C_{nml}^{(i)}$ may be mathematically viewed as the strengths of the $\vartheta(1/\sqrt{r})$ stress singularities at the crack edge most dominate for $n=1$. The $B_{nml}^{(i)}$ and $C_{nml}^{(i)}$ are evaluated in the present Ritz procedure by the clamped, hinged, and stress free boundaries of the cracked FGM parallelepiped, consequently, formulae for their evaluation may be understood from a complete stress analysis (see Appendix) of a given cracked FGM parallelepiped configuration. In the present analysis, such stress fields near the crack tip are assumed to be linearly dependent on such stress intensities, $\sqrt{2\pi}B_{nml}^{(i)}$ and $\sqrt{2\pi}C_{nml}^{(i)}$. That is, scaling $\sqrt{2\pi}B_{nml}^{(i)}$ and $\sqrt{2\pi}C_{nml}^{(i)}$ also directly scales the stress and displacement fields near the crack edge of the FGM parallelepiped,

whereas the stresses at the crack edge of the FGM parallelepiped remain unbounded.

Physically, $\sqrt{2\pi}B^{(i)}_{nml}$ and $\sqrt{2\pi}C^{(i)}_{nml}$ may be regarded as intensities of vibratory stresses through the crack edge region caused by the introduction of a crack into the FGM parallelepiped. Correspondingly, formulae for $\sqrt{2\pi}B^{(i)}_{nml}$ and $\sqrt{2\pi}C^{(i)}_{nml}$(see Appendix) may be regarded as reflecting strain redistributions for transmission of linear-elastic stress past the crack edge, even though small degrees of nonlinearity at the crack edge is embedded within the stress field and do not significantly impact the overall correctness of the present analysis. Hence, "mixed mode" cracking in FGM parallelepiped vibration is sufficient to describe the most general three-dimensional dynamic "small-scale" yielding of local crack-tip deformation and stress fields in cracked parallelepipeds. Because fracture processes of a functionally graded material may be regarded as "caused" by this surrounding crack-edge stress field nature, the intensities $\sqrt{2\pi}B^{(i)}_{nml}$ and $\sqrt{2\pi}C^{(i)}_{nml}$ may be interpreted in a generalized sense as fracture correlation coefficients in current practice. It should be noted that the intensities have units of (force) $\times$ (length)$^{-3/2}$ [33,34], and since the intensities are linear factors in elastic stress, they must be proportional to the vibratory force, and other characteristic lengths, such as crack size, i.e., determined in the present analysis by different crack length ratios (d/a and d/b), crack positions (c_x/a and c_y/b), and crack inclination angles (α) (see Fig. 1). These crack size effects addressed in the present analysis imply flaw-size influence in FGM parallelepiped vibration and fracture, suggesting that these crack size effects can be fully analyzed only if crack-edge stress singularity effects and allowing for displacement discontinuities across the crack (sufficient to describe the most general 3-D mixed modes of local crack-edge deformation and stress fields) are included.

Since the 3-D stress values near a crack edge are unbounded, a strength-of-materials approach of FGM failure prediction that the FGM fails, when the 3-D stresses exceed some critical Von-Mises measure or ultimate/yield value is inadequate. As a cracked FGM parallelepiped responds in a normal mode of vibration, in spite of the fact that the stress field near the crack tip is unbounded, the FGM parallelepiped may not necessarily fail. Beyond such critical stress limit, however, such fatigue and failure mechanisms are possible. Instead of a conventional approach of referencing a maximum FGM stress value with a critical FGM stress values, in a fracture mechanics approach FGM parallelepiped failure may be predicted by theoretically comparing the stress intensity constants, $\sqrt{2\pi}B^{(i)}_{nml}$ and $\sqrt{2\pi}C^{(i)}_{nml}$, with some critical value, thus, establishing a generalized spectral accuracy of the present Ritz methodology, especially within the crack region of a normal mode response of a cracked FGM parallelepiped. Such a critical value of generalized stress intensity may be considered a critical stress intensity or fracture toughness of the FGM. Theoretically speaking, a cracked FGM parallelepiped may fail under high-cycle fatigue and fracture as $\sqrt{2\pi}B^{(i)}_{nml}$ and $\sqrt{2\pi}C^{(i)}_{nml}$ values increase proportionately (depending on the cracked FGM parallelepiped geometry and normal mode response) beyond some critical stress intensity or fracture toughness of the FGM. Such fracture toughness is a material property, analogous to elastic homogeneous materials ultimate stress or yield stress.

In the present Ritz analysis, the material properties (*i.e.*, elastic modulus, E, Poisson's ratio, υ, and mass density, ρ) vary as a simple power law in the parallelepiped thickness (see Fig. 1), as described in Eq. (1), which exponentially depends a parameter $\hat{m}$ being the volume fraction that governs the material variation profile in the FGM parallelepiped thickness including the thickness at the crack tip. The FGM parallelepipeds under consideration are made of aluminum (Al) and ceramic (zirconia (ZrO_2) or almina (Al_2O_3)), whose material properties are given in Table 1.

The values of N_{ix}, N_{iy}, N_{iz} in Eq. (7) and $\overline{N}_i$ are assumed to vary for various i. For simplicity, $N_{ix}=\hat{N}_x$, $N_{iy}=\hat{N}_y$, $N_{iz}=\hat{N}_z$, and $\overline{N}_i=\hat{N}_c$ for $i=1$, 2, and 3 in the present study. Substituting Eqs. (7) and (9) into Eqs. (2) and (3) and minimizing the energy functional Πyield $3\times(\hat{N}_x\times\hat{N}_y\times\hat{N}_z\times\hat{N}_c\times(\hat{N}_c+3)\times\hat{N}_z)$ simultaneous algebraic solution matrix equations in Eq. (5).

3. Convergence and comparison studies

Leissa [37] described about 500 publications which appeared before 1966, and more than 1500 papers have been published since then. Relatively few published results are available for cracked rectangular plates, and most of them considered plates with simply-supported (SSSS) boundary conditions at all sides or at two opposite sides. Because exact analytical solutions exist for such plates with no crack, semi-analytical solutions [38] can be constructed for such plates with cracks along a straight line perpendicular to the simply-supported edges.

In examining the vibrations of homogeneous SSSS cracked rectangular parallelepipeds modeled as cracked plates, Lynn and Kumbasar [6] used Green's functions to represent the transverse displacements of plates, resulting in homogeneous Fredholm integral equations of the first kind, while Stahl and Keer [7] formulated such problems as dual series equations which reduced to homogeneous Fredholm integral equations of the second kind. Aggarwala and Ariel [8] applied Stahl and Keer's approach to analyze the vibration of parallelepipeds having various crack length ratios (d/a or d/b) and positions (c_y/b) along its symmetry axes. Neku [9] modified Lynn and Kumbasar's approach [6] by establishing the needed Green's functions via Levy's form of solution. Solecki [10] constructed a solution for vibrations of a cracked plate by using a Navier's solution, along with finite Fourier transformation of discontinuous functions for the displacement and slope across the crack. Recently, Khadem and Rezaee [39] used so-called modified comparison functions constructed from Levy's solution as the admissible functions of the Ritz method to analyze a SSSS rectangular cracked parallelepiped with arbitrary crack length ratio (d/a or d/b) and position (c_y/b) parallel to one side of the parallelepiped. Due to the specialized construction of their assumed Levy's solutions as admissible transverse displacement field, the Khadem and Rezaee [39] procedure can only be applied to rectangular parallelepipeds with two opposite edges simply-supported. Hirano and Okazaki [11] also developed solutions for vibrations of cracked rectangular parallelepipeds with two opposite edges simply-supported by utilizing a Levy's solution transverse displacement field and further matching the boundary conditions by means of a weighted residual method.

The convergence and comparison studies for natural frequencies of SSSS homogeneous and FGM rectangular parallelepipeds, having a side crack of various length ratios (d/a or d/b), crack positions (c/b), and crack orientation (α), are summarized now, not only to addresses the importance of using crack functions to accelerate the convergence of crack FGM parallelepiped vibrations, but also to appropriately describes the behaviors of stress singularities at the crack tip and show the discontinuities of displacement and slope crossing the crack, which are characteristics of the true solutions and the 3-D mode shapes described in Section 5. The present numerical results are compared with the published results and show better accuracy than those obtained by the Ritz method combining with different domain decomposition techniques (i.e., Yuan and Dickinson [14] and Liew et al. [15]).

The present Ritz procedure yields upper bounds to the exact values as the number of terms retained increases in the assumed hybrid series, Eq. (4), yielding in Eq. (5) a solution matrix size, $3\times(\hat{N}_x\times\hat{N}_y\times\hat{N}_z+\hat{N}_c\times(\hat{N}_c+3)\times\hat{N}_z)$. A convergence study

Table 2
Convergence of $\omega(b^2/h)\sqrt{\rho/E}$ for a homogeneous, cracked SSSS rectangular parallelepiped modeled as a thin plate with a horizontal side crack[@] ($a/b=2.0$, $h/b=0.01$, $c_y/b=0.5$, $d/a=0.5$, $\alpha=0^\circ$).

Mode no.	Crack functions ($\hat{N}_c$)	Polynomial solution size ($I\times J$) [@] [ ] $\hat{N}_z=2$; ( ) $\hat{N}_z=3$; { } $\hat{N}_z=4$						Stahl & Keer* [7] Huang et al. [+][2,3]
		4×4	5×5	6×6	7×7	8×8	9×9	
1	0	[4.132]	[4.132]	[4.131]	[4.131]	[4.131]	[4.131]	3.05* 3.053[+]
		(3.733)	(3.733)	(3.733)	(3.733)	(3.733)	(3.733)	
		{3.733}	{3.733}	{3.733}	{3.733}	{3.733}	{3.733}	
	2	[3.877]	[3.648]	[3.618]	[3.464]	[3.452]	[3.368]	
		(3.551)	(3.384)	(3.363)	(3.247)	(3.238)	(3.173)	
		{3.551}	{3.383}	{3.363}	{3.247}	{3.238}	{3.173}	
	4	[3.234]	[3.234]	[3.220]	[3.217]	[3.217]	[3.216]	
		(3.065)	(3.057)	(3.054)	(3.052)	(3.051)	(3.051)	
		{3.064}	{3.057}	{3.053}	{3.051}	{3.051}	{3.050}	
	5	[3.225]	[3.217]	[3.217]	[3.216]	[3.216]	[3.215]	
		(3.058)	(3.052)	(3.051)	(3.051)	(3.050)	(3.050)	
		{3.057}	{3.052}	{3.051}	{3.050}	{3.050}	{3.049}	
	6	[3.220]	[3.216]	[3.216]	[3.215]	[3.215]	[3.214]	
		(3.054)	(3.051)	(3.050)	(3.050)	(3.050)	(3.049)	
		{3.054}	{3.050}	{3.050}	{3.049}	{3.049}	{3.048}	
2	0	[7.198]	[6.618]	[6.618]	[6.609]	[6.609]	[6.609]	5.507* 5.506[+]
		(6.539)	(5.981)	(5.980)	(5.972)	(5.972)	(5.971)	
		{6.539}	{5.980}	{5.980}	{5.971}	{5.971}	{5.971}	
	2	[6.919]	[6.209]	[6.189]	[6.102]	[6.096]	[6.060]	
		(6.347)	(5.699)	(5.685)	(5.614)	(5.609)	(5.578)	
		{6.346}	{5.699}	{5.685}	{5.613}	{5.609}	{5.578}	
	4	[5.840]	[5.799]	[5.780]	[5.773]	[5.769]	[5.767]	
		(5.554)	(5.517)	(5.512)	(5.507)	(5.506)	(5.505)	
		{5.554}	{5.516}	{5.512}	{5.506}	{5.506}	{5.505}	
	5	[5.779]	[5.765]	[5.761]	[5.759]	[5.758]	[5.757]	
		(5.539)	(5.508)	(5.505)	(5.504)	(5.504)	(5.504)	
		{5.539}	{5.507}	{5.504}	{5.504}	{5.504}	{5.503}	
	6	[5.765]	[5.761]	[5.758]	[5.758]	[5.756]	[5.756]	
		(5.532)	(5.506)	(5.504)	(5.504)	(5.504)	(5.503)	
		{5.532}	{5.505}	{5.504}	{5.503}	{5.503}	{5.503}	
3	0	[13.75]	[13.74]	[10.84]	[10.84]	[10.74]	[10.74]	5.570* 5.570[+]
		(12.78)	(12.61)	(9.801)	(9.799)	(9.703)	(9.703)	
		{12.77}	{12.61}	{9.801}	{9.798}	{9.703}	{9.703}	
	2	[13.51]	[12.93]	[10.75]	[10.74]	[10.64]	[10.63]	
		(12.51)	(11.90)	(9.747)	(9.733)	(9.642)	(9.637)	
		{12.50}	{11.90}	{9.747}	{9.732}	{9.642}	{9.636}	
	4	[6.027]	[5.973]	[5.967]	[5.960]	[5.960]	[5.958]	
		(5.631)	(5.598)	(5.584)	(5.578)	(5.574)	(5.573)	
		{5.630}	{5.597}	{5.583}	{5.577}	{5.573}	{5.572}	
	5	[6.006]	[5.961]	[5.957]	[5.956]	[5.956]	[5.956]	
		(5.583)	(5.571)	(5.568)	(5.566)	(5.564)	(5.564)	
		{5.582}	{5.570}	{5.566}	{5.565}	{5.563}	{5.562}	
	6	[5.996]	[5.958]	[5.956]	[5.956]	[5.956]	[5.955]	
		(5.570)	(5.567)	(5.564)	(5.564)	(5.562)	(5.562)	
		{5.569}	{5.566}	{5.563}	{5.562}	{5.561}	{5.560}	
4	0	[17.49]	[14.09]	[14.09]	[14.04]	[14.04]	[14.04]	9.336* 9.336[+]
		(16.04)	(12.74)	(12.74)	(12.69)	(12.69)	(12.68)	
		{16.04}	{12.74}	{12.73}	{12.68}	{12.68}	{12.68}	
	2	[14.32]	[13.34]	[12.51]	[12.45]	[12.10]	[12.07]	
		(13.40)	(12.26)	(11.59)	(11.54)	(11.27)	(11.24)	
		{13.40}	{12.26}	{11.59}	{11.54}	{11.27}	{11.24}	
	4	[11.44]	[10.32]	[10.16]	[10.15]	[10.12]	[10.12]	
		(10.52)	(9.545)	(9.382)	(9.370)	(9.343)	(9.341)	
		{10.52}	{9.544}	{9.381}	{9.369}	{9.342}	{9.340}	
	5	[10.77]	[10.13]	[10.12]	[10.11]	[10.10]	[10.10]	
		(9.884)	(9.359)	(9.349)	(9.341)	(9.333)	(9.333)	
		{9.883}	{9.359}	{9.348}	{9.340}	{9.332}	{9.332}	
	6	[10.62]	[10.11]	[10.11]	[10.10]	[10.10]	[10.10]	
		(9.766)	(9.341)	(9.339)	(9.332)	(9.332)	(9.331)	
		{9.765}	{9.340}	{9.338}	{9.331}	{9.331}	{9.330}	
5	0	[19.96]	[16.57]	[16.57]	[16.51]	[16.51]	[16.51]	12.76* 12.87[+]
		(18.25)	(14.97)	(14.97)	(14.92)	(14.92)	(14.92)	
		{18.25}	{14.97}	{14.97}	{14.92}	{14.92}	{14.92}	
	2	[18.51]	[15.46]	[15.30]	[15.24]	[15.15]	[15.15]	
		(17.01)	(14.06)	(13.90)	(13.84)	(13.76)	(13.75)	
		{17.01}	{14.06}	{13.90}	{13.84}	{13.75}	{13.75}	
	4	[14.73]	[14.65]	[14.57]	[14.50]	[14.48]	[14.46]	
		(13.33)	(13.27)	(13.21)	(13.15)	(13.14)	(13.13)	
		{13.33}	{13.27}	{13.21}	{13.15}	{13.14}	{13.13}	

Table 2 (*continued*)

Mode no.	Crack functions ($\hat{N}_c$)	Polynomial solution size ($I \times J$) @[ ]$\hat{N}_z=2$; ( )$\hat{N}_z=3$; { } $\hat{N}_z=4$						Stahl & Keer* [7] Huang et al. +[2,3]
		4×4	5×5	6×6	7×7	8×8	9×9	
	5	[14.11]	[13.98]	[13.95]	[13.94]	[13.93]	[13.93]	
		(12.88)	(12.81)	(12.79)	(12.78)	(12.78)	(12.77)	
		{12.88}	{12.81}	{12.79}	{12.78}	{12.77}	{12.77}	
	6	[13.97]	[13.93]	[13.92]	[13.92]	[13.91]	[13.91]	
		(12.79)	(12.77)	(12.77)	(12.76)	(12.76)	(12.76)	
		{12.79}	{12.77}	{12.76}	{12.76}	{12.76}	{12.76}	

was conducted for rectangular parallelepipeds modeled as thick plates with different h/b to verify the correctness of the proposed solutions. The rectangular parallelepipeds are assumed simply-supported on the faces $x=0$, $x=a$, $y=0$, and $y=b$. The corresponding geometric boundary conditions are $U_2 = U_3 = 0$ at $x=0$ and $x=a$, and $U_1 = U_3 = 0$ at $y=0$ and $y=b$. Thus, in Eq. (9), $g_1(x, y, z) = y(b-y)$, $g_2(x, y, z) = x(a-x)$, and $g_3(x, y, z) = x(a-x)y(b-y)$. Poisson's ratio ($\nu$) is set equal to 0.3 for the homogeneous parallelepipeds analyzed. Table 2 summarizes the convergence studies of the first five non-dimensional frequency parameters for a rectangular ($a/b=2$), homogeneous SSSS parallelepiped modeled as a thin plate ($h/b=0.01$) with a side crack, having position ratio, $c_y/b=0.5$, and having crack length ratio, $d/a=0.5$, and crack orientation horizontally at $\alpha=0^\circ$. Posted values of the first five $\omega(b^2/h)\sqrt{\rho/E}$ were obtained using increasing orthogonal polynomial solution size, $\hat{N}_x \times \hat{N}_y = (4\times4), (5\times5), \ldots, (9\times9)$, crack functions, $\hat{N}_c=0$, 2, 4, 5, 6, and algebraic polynomials solution size, $\hat{N}_z=2$, 3, 4, assuming correspondingly first-order, second-order, or cubic-order transverse shear deformation through the parallelepiped thickness. For an intact SSSS parallelepiped, using only polynomials as assumed displacement fields in the present Ritz procedure gives insufficiently converged solutions, as the polynomial solution sizes, $\hat{N}_x \times \hat{N}_y$ and $\hat{N}_z$ increases. Augmenting the assumed displacement of admissible polynomials with crack functions, *i.e.*, for a solution matrix size, $3 \times (\hat{N}_x \times \hat{N}_y \times \hat{N}_z + \hat{N}_c \times (\hat{N}_c+3) \times \hat{N}_z)$, yields upper bounds to converge to the values in excellent agreement with the published results of Stahl and Keer [7] and Huang and Leissa [2,3] using the classical thin plate theory (see Table 2). Stahl and Keer [7] used an accurate Fredholm integration approach, while Huang and Leissa [2,3] used the Ritz method using classical thin-plate theory assuming hybrid series of plate's transverse displacement field of algebraic polynomials and special corner functions that appropriately described the stress singularities at the crack tip and discontinuities of transverse displacement and slope crossing the crack.

It can be seen in Table 2 that using an orthogonal polynomial solution size, $\hat{N}_x \times \hat{N}_y = 9\times9$, corner functions, $\hat{N}_c=6$, and algebraic polynomial solution size, $\hat{N}_z=4$, taking on cubic-order transverse shear flexibility through the parallelepiped thickness (for a 1620-term solution matrix size) yields converged frequencies at least to three significant figures, slightly lower than those solutions obtained using the classical thin plate theory (Stahl and Keer [7] and Huang and Leissa [2,3]), mainly because of the effects of shear deformation and rotary inertia inherent to the present 3-D solutions. As contrasted in Table 2, the 3-D solutions obtained assuming constant transverse shear flexibility through the parallelepiped thickness ($\hat{N}_z=2$) are markedly insufficient in regards to overall solution accuracy compared to 3-D solutions obtained assuming linear or parabolic transverse shear flexibility through the parallelepiped thickness ($\hat{N}_z=3$ or 4).

Table 3 describes the convergence of the first five non-dimensional frequencies for SSSS square FGM parallelepiped modeled as a moderately thick ($h/b=0.1$), square FGM plate having a horizontal side crack ($\alpha=0^\circ$) positioned at $c_y/b=0.5$ with crack length ratio, $d/a=0.5$. The parallelepiped is made of aluminum (Al) and alumina (Al_2O_3), and the material properties linearly vary ($\hat{m}=1$ in Eq. (1)) along the thickness direction. The non-dimensional frequency parameter, $\omega(b^2/h)\sqrt{\rho_c/E_c}$, in which subscript "$c$" refers to a reference ceramic material, is employed. Reported values of $(\omega)(b^2/h)\sqrt{\rho_c/E_c}$ were obtained using increasing orthogonal polynomial solution size, $\hat{N}_x \times \hat{N}_y = (4\times4), (5\times5), \ldots, (9\times9)$, crack functions, $\hat{N}_c=0$, 2, 4, 5, 6, and algebraic polynomial solution size, $\hat{N}_z=4$, 5, 6, taking on correspondingly 3rd, 4th, or 5th higher-order transverse shear deformation through the parallelepiped thickness. In contrast to conventional laminated composite materials, which have abrupt change in material properties, causing large interlaminar stresses and delaminations across the interface between differing material layers with different materials, functionally graded materials do not have these adverse interlamination stress and delamination effects, as material properties of functionally graded materials vary continuously by gradually changing the volume fraction of constituent properties.

Mac and Huang [19] employed element-free *kp*-Ritz method based on Mindlin plate theory, reporting the first four non-dimensional frequencies $\omega(b^2/h)\sqrt{\rho/E}$ of an intact SSSS FGM plate, as follows: Mode 1: 4.3474, Mode 2: 10.416, Mode 3: 10.416, Mode 4: 15.936. These Mac and Huang [19] intact Mindlin SSSS FGM plate solutions appear to be in proximity agreement with the predicted 3-D solutions of a cracked SSSS FGM parallelepiped modeled as a moderately thick, cracked FGM plate ($h/b=0.1$) using no crack functions ($\hat{N}_c=0$) reported in Table 3 (that is, Mode 1: 4.426, Mode 2: 10.63, Mode 3: 10.63, Mode 4: 16.20, Mode 5: 16.20), albeit the present 3-D solutions using no crack functions ($\hat{N}_c=0$) appear to be converging to slightly higher upper-bounds on the exact solutions above the upper-bound Mindlin FGM SSSS plate solutions of Mac and Huang [19]. However, by incorporating crack functions into the present 3-D calculations, one substantially enhances the convergence of solutions. Indeed, using an orthogonal polynomial solution size, $\hat{N}_x \times \hat{N}_y = 9\times9$, corner functions, $\hat{N}_c=6$, and algebraic polynomial solution size, $\hat{N}_z=6$, assuming 5th-order transverse shear flexibility through the parallelepiped thickness (for a 2430-term solution matrix size) yields 3-D solutions posted in Table 3 that can be described as exact to at least three significant figures. The Mac and Huang [19] Mindlin SSSS FGM plate solutions are indeed not in close agreement with the predicted 3-D solutions of a cracked SSSS FGM parallelepiped modeled as a moderately thick FGM plate using six crack functions ($\hat{N}_c=6$) reported in Table 3, which are as follows: Mode 1: 4.270, Mode 2: 9.963, Mode 3: 10.34, Mode 4: 13.95, Mode 5: 14.45, predicted using four or six terms in the parallelepiped thickness (z) direction. Moreover, due to the presence of the horizontal crack, the converged cracked

Table 3
Convergence of $\omega(b^2/h)\sqrt{\rho_c/E_c}$ for a Al/Al_2O_3 FGM cracked SSSS square parallelepiped modeled as a Al/Al_2O_3 FGM SSSS square, moderately thick plate with a horizontal side crack[@] ($h/b=0.1$, $c_y/b=0.5$, $d/a=0.5$, $\alpha=0^\circ$, $\hat{m}=1$).

Mode no.	Crack functions ($\hat{N}_c$)	Polynomial solution size ($I\times J$) [@] [ ] $\hat{N}_z=4$; ( ) $\hat{N}_z=5$; { } $\hat{N}_z=6$					
		4×4	5×5	6×6	7×7	8×8	9×9
1	0	[4.427]	[4.427]	[4.426]	[4.426]	[4.426]	[4.426]
		(4.427)	(4.427)	(4.426)	(4.426)	(4.426)	(4.426)
		{4.427}	{4.427}	{4.426}	{4.426}	{4.426}	{4.426}
	2	[4.304]	[4.292]	[4.289]	[4.284]	[4.283]	[4.281]
		(4.303)	(4.292)	(4.289)	(4.284)	(4.823)	(4.280)
		{4.303}	{4.292}	{4.289}	{4.284}	{4.283}	{4.280}
	4	[4.275]	[4.273]	[4.273]	[4.272]	[4.272]	[4.271]
		(4.275)	(4.273)	(4.273)	(4.272)	(4.271)	(4.271)
		{4.275}	{4.273}	{4.273}	{4.272}	{4.271}	{4.271}
	5	[4.274]	[4.271]	[4.271]	[4.271]	[4.271]	[4.270]
		(4.273)	(4.271)	(4.271)	(4.271)	(4.270)	(4.270)
		{4.273}	{4.271}	{4.271}	{4.271}	{4.270}	{4.270}
	6	[4.272]	[4.271]	[4.271]	[4.270]	[4.270]	[4.270]
		(4.272)	(4.271)	(4.270)	(4.270)	(4.270)	(4.270)
		{4.272}	{4.271}	{4.270}	{4.270}	{4.270}	{4.270}
2	0	[12.49]	[10.66]	[10.66]	[10.63]	[10.63]	[10.63]
		(12.49)	(10.66)	(10.66)	(10.63)	(10.63)	(10.63)
		{12.49}	{10.66}	{10.66}	{10.63}	{10.63}	{10.63}
	2	[10.36]	[10.16]	[10.12]	[10.10]	[10.08]	[10.08]
		(10.36)	(10.15)	(10.12)	(10.10)	(10.08)	(10.08)
		{10.36}	{10.15}	{10.12}	{10.10}	{10.08}	{10.07}
	4	[9.994]	[9.987]	[9.978]	[9.974]	[9.970]	[9.969]
		(9.994)	(9.986)	(9.977)	(9.973)	(9.969)	(9.968)
		{9.993}	{9.986}	{9.976}	{9.973}	{9.969}	{9.968}
	5	[9.981]	[9.977]	[9.971]	[9.969]	[9.967]	[9.966]
		(9.980)	(9.976)	(9.970)	(9.968)	(9.966)	(9.965)
		{9.980}	{9.975}	{9.970}	{9.968}	{9.965}	{9.965}
	6	[9.972]	[9.970]	[9.968]	[9.966]	[9.965]	[9.964]
		(9.972)	(9.970)	(9.967)	(9.965)	(9.964)	(9.963)
		{9.971}	{9.969}	{9.966}	{9.965}	{9.963}	{9.963}
3	0	[12.49]	[10.66]	[10.66]	[10.63]	[10.63]	[10.63]
		(12.49)	(10.66)	(10.66)	(10.63)	(10.63)	(10.63)
		{12.49}	{10.66}	{10.66}	{10.63}	{10.63}	{10.63}
	2	[10.77]	[10.39]	[10.38]	[10.36]	[10.36]	[10.35]
		(10.77)	(10.39)	(10.38)	(10.36)	(10.36)	(10.35)
		{10.77}	{10.39}	{10.38}	{10.36}	{10.36}	{10.35}
	4	[10.36]	[10.35]	[10.34]	[10.34]	[10.34]	[10.34]
		(10.35)	(10.35)	(10.34)	(10.34)	(10.34)	(10.34)
		{10.35}	{10.35}	{10.34}	{10.34}	{10.34}	{10.34}
	5	[10.35]	[10.34]	[10.34]	[10.34]	[10.34]	[10.34]
		(10.35)	(10.34)	(10.34)	(10.34)	(10.34)	(10.34)
		{10.35}	{10.34}	{10.34}	{10.34}	{10.34}	{10.34}
	6	[10.34]	[10.34]	[10.34]	[10.34]	[10.34]	[10.34]
		(10.34)	(10.34)	(10.34)	(10.34)	(10.34)	(10.34)
		{10.34}	{10.34}	{10.34}	{10.34}	{10.34}	{10.34}
4	0	[16.20]	[16.20]	[16.20]	[16.20]	[16.20]	[16.20]
		(16.20)	(16.20)	(16.20)	(16.20)	(16.20)	(16.20)
		{16.20}	{16.20}	{16.20}	{16.20}	{16.20}	{16.20}
	2	[14.02]	[14.01]	[14.00]	[14.00]	[13.99]	[13.99]
		(14.02)	(14.01)	(14.00)	(14.00)	(13.99)	(13.99)
		{14.02}	{14.01}	{14.00}	{14.00}	{13.99}	{13.99}
	4	[13.96]	[13.95]	[13.95]	[13.95]	[13.95]	[13.95]
		(13.96)	(13.95)	(13.95)	(13.95)	(13.95)	(13.95)
		{13.96}	{13.95}	{13.95}	{13.95}	{13.95}	{13.95}
	5	[13.95]	[13.95]	[13.95]	[13.95]	[13.95]	[13.95]
		(13.95)	(13.95)	(13.95)	(13.95)	(13.95)	(13.95)
		{13.95}	{13.95}	{13.95}	{13.95}	{13.95}	{13.95}
	6	[13.95]	[13.95]	[13.95]	[13.95]	[13.95]	[13.95]
		(13.95)	(13.95)	(13.95)	(13.95)	(13.95)	(13.95)
		{13.95}	{13.95}	{13.95}	{13.95}	{13.95}	{13.95}
5	0	[16.20]	[16.20]	[16.20]	[16.20]	[16.20]	[16.20]
		(16.20)	(16.20)	(16.20)	(16.20)	(16.20)	(16.20)
		{16.20}	{16.20}	{16.20}	{16.20}	{16.20}	{16.20}
	2	[16.20]	[14.95]	[14.88]	[14.83]	[14.79]	{14.78}
		(16.20)	(14.95)	(14.88)	(14.83)	(14.79)	(14.78)
		{16.20}	{14.95}	{14.88}	{14.83}	{14.79}	{14.78}
	4	[14.51]	[14.49]	[14.48]	[14.47]	[14.46]	[14.46]
		(14.51)	(14.49)	(14.48)	(14.46)	(14.46)	(14.46)
		{14.50}	{14.49}	{14.47}	{14.46}	{14.46}	{14.46}

Table 3 (*continued*)

Mode no.	Crack functions ($\hat{N}_c$)	Polynomial solution size $(I\times J)$ @[ ]$\hat{N}_z=4$; ( )$\hat{N}_z=5$; { }$\hat{N}_z=6$					
		4×4	5×5	6×6	7×7	8×8	9×9
	5	[14.48]	[14.47]	[14.46]	[14.46]	[14.45]	[14.45]
		(14.48)	(14.47)	(14.46)	(14.46)	(14.45)	(14.45)
		{14.48}	{14.47}	{14.46}	{14.45}	{14.45}	{14.45}
	6	[14.46]	[14.46]	[14.46]	[14.45]	[14.45]	[14.45]
		(14.46)	(14.46)	(14.45)	(14.45)	(14.45)	(14.45)
		{14.46}	{14.46}	{14.45}	{14.45}	{14.45}	{14.45}

SSSS FGM parallelepiped solutions possess no repeated frequency Modes 2–3 and Modes 4–5.

Symmetric and anti-symmetric, $\omega(b^2/h)\sqrt{\rho/E}$, associated to independent normal mode responses are obtained, when the cracked FGM parallelepiped vibrates symmetrically and anti-symmetrically (as seen in Figs. 2–6 to be discussed in more detail subsequently in Section 5). When the vibratory stress is in a direction perpendicular to the crack surface, then the normal mode response sees an opening mode of the crack. When the vibratory stress is parallel to the crack surface, then the normal mode response sees a shearing or sliding mode of the crack. In some coupled normal mode responses, the vibratory stress creates both opening and shearing/sliding mode components of the crack inducing a mixed modal vibration along the crack. Each of these cracked normal response negate any kinds of repeated mode $\omega(b^2/h)\sqrt{\rho/E}$ associated with an intact FGM parallelepiped (Mac and Huang [19]).

To the authors' knowledge, there are no published results on the vibrations of cracked parallelepipeds modeled as plates. To further verify the accuracy of the present 3-D vibration solutions, Table 4 contrasts $\omega(b^2/h)\sqrt{\rho/E}$ predictions obtained by various theories for SSSS homogeneous cracked square parallelepipeds with horizontal side cracks ($\alpha=0^\circ$) having various length ratios (d/a) and positioned at $c_y/b=0.5$. The present 3-D Ritz $\omega(b^2/h)\sqrt{\rho/E}$ solutions are posted against $\omega(b^2/h)\sqrt{\rho/E}$ calculated for homogeneous cracked parallelepipeds modeled as classical thin plates and Mindlin plates. Square parallelepipeds modeled as plates having three different thickness-length ratios ($h/b=0.002$ (very thin), 0.05 (thin), 0.1 (moderately thick)) and two different horizontal crack length ratios ($d/a=0.2$ and 0.4) are considered. Only $\omega(b^2/h)\sqrt{\rho/E}$ for the out-of-plane modes are listed in Table 4. Huang and Leissa [2,3] applied the Ritz method with the admissible functions, including a set of crack functions possessing admissibility analogous to that of the present 3-D analysis, yet suitable for incorporation with classical thin plate theory, while Li [4] employed a similar methodology based on Mindlin plate theory with the shear correction factor equal to $\pi^2/12$. The present 3-D results for very thin plates ($h/b=0.002$) were obtained using orthogonal polynomial solution size, $\hat{N}_x\times\hat{N}_y=9\times9$ (Eq. (7)), crack functions, $\hat{N}_c=6$ (Eq. (9)), and algebraic polynomial solution size (Eq. (7)), $\hat{N}_z=4$ and 6, taking on correspondingly a cubic-order and 5th-order transverse shear deformation through the parallelepiped thickness. This yields a 1620-term solution matrix size for $\hat{N}_x\times\hat{N}_y=9\times9$, $\hat{N}_c=6$, $\hat{N}_z=4$, and a 2430-term solution matrix size for $\hat{N}_x\times\hat{N}_y=9\times9$, $\hat{N}_c=6$, $\hat{N}_z=4$.

Considering stress singularities in cracked parallelepiped vibration in flexure, a first-order (Mindlin) shear deformable analysis [4] should yield lower $\omega(b^2/h)\sqrt{\rho/E}$ values than classical thin-plate solutions [2,3]. Shear deformation reduces the $\omega(b^2/h)\sqrt{\rho/E}$ solutions. Rotary inertia reduces the higher modes of $\omega(b^2/h)\sqrt{\rho/E}$. As $\omega(b^2/h)\sqrt{\rho/E}$ is non-dimensionalized with respect to ρ, E, and explicitly, h, comparisons in Table 4 between first-order (Mindlin) and higher-order shear deformable [4] and classical thin-plate $\omega(b^2/h)\sqrt{\rho/E}$ solutions [2,3] are largely independent of parallelepiped shape being square ($a/b=1$) or rectangular ($a/b\neq1$), showing primarily influences of crack length ratio (d/a) at position ($c_y/b=0.5$) and horizontal orientation ($\alpha=0^\circ$). As the plate becomes thicker or in Table 4 as the frequency mode number increases, distinctions in Table 4 between shear deformable [4] and classical plate [2,3] $\omega(b^2/h)\sqrt{\rho/E}$ solutions are more apparent.

As expected, the differences between the frequencies of very thin plates ($h/b=0.002$) obtained based on the classical thin plate theory [2,3] and Mindlin plate theory [4] are negligible, and both are consistent with the present 3-D elasticity-based predicted solutions up to at least three significant figures. For the thin ($h/b=0.05$) and moderately thick ($h/b=0.1$) plates, the predicted $\omega(b^2/h)\sqrt{\rho/E}$ solutions based on the classical thin plate theory are considerably stiffer than the predicted shear deformable $\omega(b^2/h)\sqrt{\rho/E}$ solutions based on Mindlin plate theory [4] and present 3-D elasticity theory, especially for homogeneous SSSS parallelepipeds modeled as moderately thick plates ($h/b=0.1$) and for the higher $\omega(b^2/h)\sqrt{\rho/E}$ modes. The homogeneous SSSS parallelepiped $\omega(b^2/h)\sqrt{\rho/E}$ solutions modeled from shear deformable Mindlin plate theory [4] are slightly over-correcting in reducing the classical thin plate theory $\omega(b^2/h)\sqrt{\rho/E}$ solutions [2,3] for transverse shear effects compared to the corrections in reducing the classical thin plate theory $\omega(b^2/h)\sqrt{\rho/E}$ solutions for transverse shear effects inherent to the present 3-D $\omega(b^2/h)\sqrt{\rho/E}$ solutions. Percentage differences between the shear deformable Mindlin $\omega(b^2/h)\sqrt{\rho/E}$ solutions and the present 3-D $\omega(b^2/h)\sqrt{\rho/E}$ solutions are less than 1%. Generally speaking, this 1% difference does not significantly increase with increasing crack length ratio (d/a).

4. Numerical results and discussion

The vibrations of cracked rectangular parallelepipeds with arbitrary boundary conditions are typically modeled as plates using both the finite element method and the Ritz method. Qian et al. [12] developed a finite element solution by deriving the stiffness matrix for an element including the crack tip from the integration of the stress intensity factor. Krawczuk [13] proposed a solution similar to that of Qian et al. [12], except that the stiffness matrix for an element including the crack tip was expressed in a closed form. Yuan and Dickinson [14] decomposed a rectangular plate into several domains and introduced artificial springs at the interconnecting boundaries between the domains so that the Ritz method with regular admissible functions can be applied to find the solutions. Similar to the approach used by Yuan and Dickinson [14], Liew et al. [15] required the continuities of displacement and slope in a sense of integration along the interconnecting boundaries. In the approach of Liew et al., the continuities of displacement and slope are not satisfied at every point along the interconnecting boundaries. Notably, the

a

$\hat{m}$	d/b	Mode Number 1	2	3	4	5
0	0	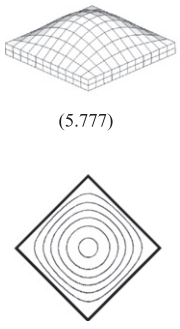 (5.777)	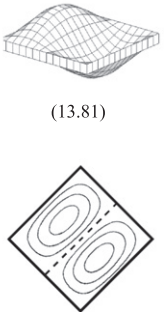 (13.81)	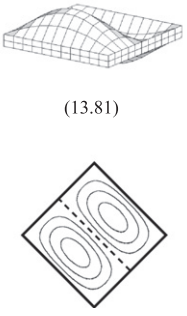 (13.81)	* 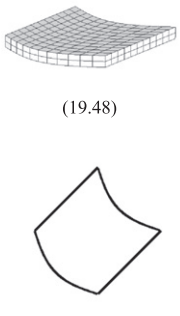 (19.48)	* 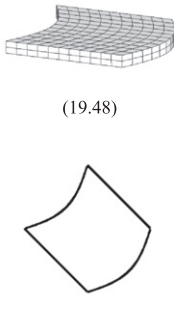 (19.48)

b

$\hat{m}$	d/b	Mode Number 1	2	3	4	5
0	0.2	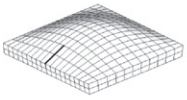 (5.758)	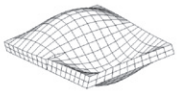 (13.72)	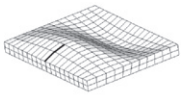 (13.74)	* 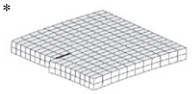 (18.57)	* 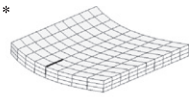 (19.48)
	0.5	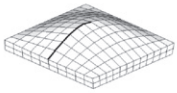 (5.385)	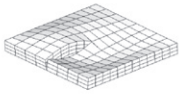 (11.40)	 (13.35)	* 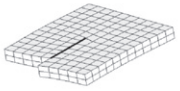 (16.19)	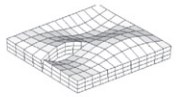 (17.35)

c

α	c_y/b	d/b	Mode No. 1	2	3	4	5
0°	0.5	0.2	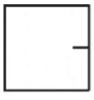 (5.962)	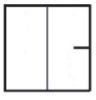 (14.89)	 (14.93)	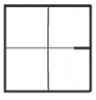 (23.84)	 (29.62)
		0.5	 (5.644)	 (13.14)	 (14.50)	 (19.49)	 (26.65)

Fig. 2. (a) Mode shapes, nodal patterns and $\omega(b^2/h)\sqrt{\rho/E}$ for a SSSS homogeneous square parallelepiped modeled as a moderately thick plate ($c_x/a=0$, $d/b=0$, $h/b=0.1$); (b) mode shapes, nodal patterns and $\omega(b^2/h)\sqrt{\rho_c/E_c}$ for SSSS homogeneous cracked square parallelepipeds modeled as moderately thick cracked plates ($c_x/a=0$, $d/b=0.2,0.5$, $h/b=0.1$, $c_y/b=0.5$, $\alpha=0^\circ$) and (c) nodal patterns and $\omega(b^2/h)\sqrt{\rho/E}$ for SSSS homogeneous cracked square parallelepipeds modeled as classically-thin cracked plates (Huang and Leissa [2]) ($\hat{m}=0$, $d/b=0.2,0.5$, $h/b=0.01$, $c_y/b=0.5$, $\alpha=0^\circ$).

solutions of Yuan and Dickinson [14] and Liew et al. [15] destroy the good characteristics of providing upper-bound solutions for vibration frequencies, normally associated with the Ritz method.

These published solutions, except for the finite element solutions, by no means address the stress singularities at the crack terminus edge of FGM parallelepipeds. Addressed in this section is 3-D elasticity-based Ritz predictions including such stress singularities to investigate the vibrations of side-cracked rectangular FGM parallelepipeds, particularly bringing forth the possible discontinuities of displacement and slope across the crack. Since a crack is a special case

a

$\hat{m}$	d/b	Mode Number 1	2	3	4	5
5	0	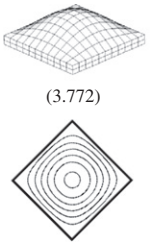 (3.772)	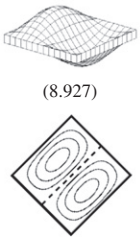 (8.927)	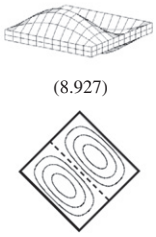 (8.927)	* 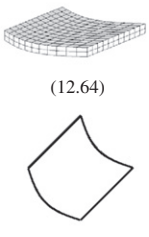 (12.64)	* 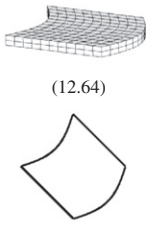 (12.64)

b

$\hat{m}$	d/b	Mode Number 1	2	3	4	5
5	0.2	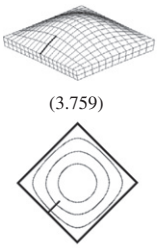 (3.759)	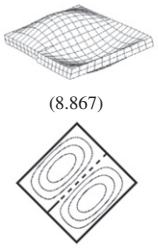 (8.867)	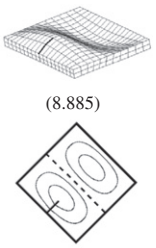 (8.885)	* 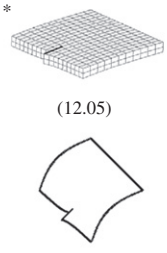 (12.05)	* 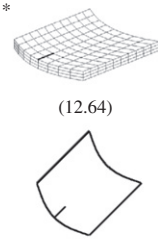 (12.64)
	0.5	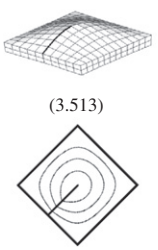 (3.513)	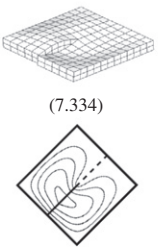 (7.334)	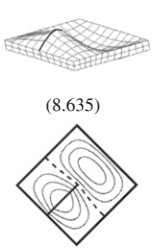 (8.635)	* 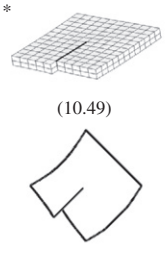 (10.49)	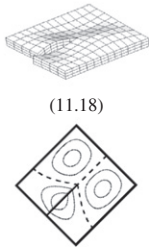 (11.18)

c

$\hat{m}$	d/b	Mode 1	2	3	4	5
5	0	 (3.768)	 (8.909)	 (8.909)	 (12.64)	 (12.64)
	0.2	 (3.756)	 (8.851)	 (8.867)	 (12.04)	 (12.64)
	0.5	 (3.511)	 (7.379)	 (8.621)	 (10.49)	 (11.17)

Fig. 3. (a) Mode shapes, nodal patterns and $\omega(b^2/h)\sqrt{\rho_c/E_c}$ for a SSSS square Al/Al_2O_3 FGM parallelepiped modeled as a moderately thick Al/Al_2O_3 FGM plate ($\hat{m}=5$, $d/b=0$, $h/b=0.1$); (b) mode shapes, nodal patterns and $\omega(b^2/h)\sqrt{\rho_c/E_c}$ for SSSS cracked Al/Al_2O_3 FGM square parallelepipeds modeled as moderately thick cracked Al/Al_2O_3 FGM plates ($\hat{m}=5$, $d/b=0.2,0.5$, $h/b=0.1$, $c_y/b=0.5$, $\alpha=0^\circ$) and (c) nodal patterns and $\hat{m}$for SSSS cracked Al/Al_2O_3 FGM square parallelepipeds modeled as a moderately thick cracked Al/Al_2O_3 FGM plate using Reddy thick plate theory (Huang et al. [32]) ($\hat{m}=5$, $d/b=0,0.2,0.5$, $h/b=0.1$, $c_y/b=0.5$, $\alpha=0^\circ$).

of a V-notch, the asymptotic solutions (or crack functions) derived by Williams [31] were shown to be particularly effective for this, according to Kim and Jung [40] who applied this methodology to investigate the vibrations of rhombic plates with V-notches, and according to the authors' experiences in studying vibrations of a circular plate with a V-notch (Leissa et al. [41]). However, Huang and Leissa [2,3] have demonstrated that using Williams' asymptotic solutions and regular polynomials as admissible functions does not yield as rapidly convergent solutions for parallelepipeds having a deep (d/a or $d/b=0.5$) compared to a shallow (d/a or $d/b=0.2$) side crack.

The present 3-D Ritz technique is used to predict $\omega(b^2/h)\sqrt{\rho_c/E_c}$ for FGM rectangular parallelepipeds with various

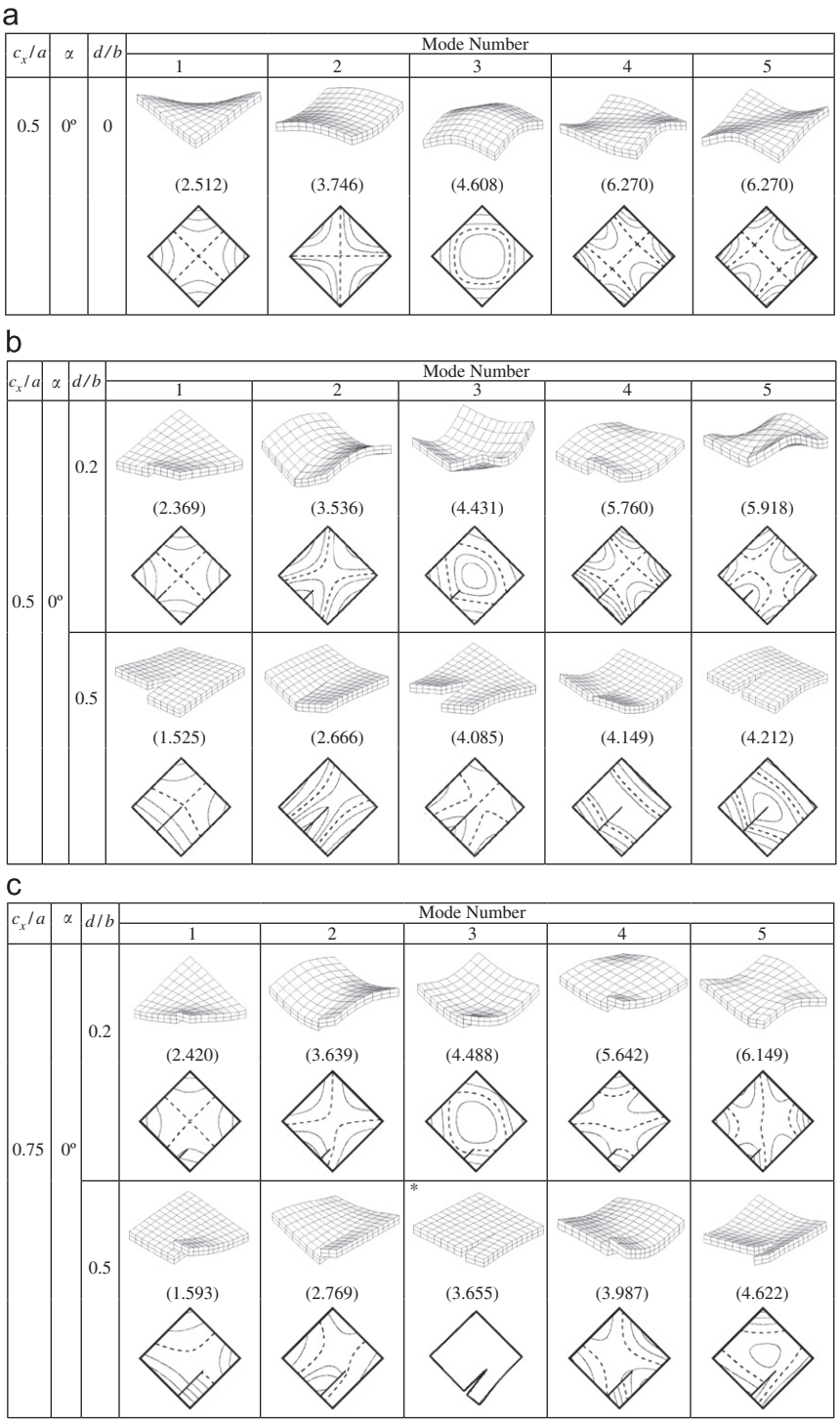

Fig. 4. (a) Mode shapes, nodal patterns and $\omega(b^2/h)\sqrt{\rho_c/E_c}$ for a FFFF square Al/Al_2O_3 FGM parallelepiped modeled as a moderately thick Al/Al_2O_3 FGM plate ($\hat{m}=5$, $d/b=0$, $h/b=0.1$, $c_x/a=0.5$, $\alpha=0^\circ$); (b) mode shapes, nodal patterns and $\omega(b^2/h)\sqrt{\rho/E}$ for FFFF cracked square Al/Al_2O_3 FGM parallelepipeds modeled as moderately thick cracked Al/Al_2O_3 FGM plates ($\hat{m}=5$, $d/b=0.2,0.5$, $h/b=0.1$, $c_x/a=0.5$, $\alpha=0^\circ$); (c) mode shapes, nodal patterns and $\omega(b^2/h)\sqrt{\rho/E}$ for FFFF cracked square Al/Al_2O_3 FGM parallelepipeds modeled as moderately thick cracked Al/Al_2O_3 FGM plates ($\hat{m}=5$, $d/b=0.2,0.5$, $h/b=0.1$, $c_x/a=0.75$, $\alpha=0^\circ$); (d) mode shapes, nodal patterns and $\omega(b^2/h)\sqrt{\rho/E}$ for FFFF cracked square Al/Al_2O_3 FGM parallelepipeds modeled as moderately thick cracked Al/Al_2O_3 FGM plates ($\hat{m}=5$, $d/b=0.2,0.5$, $h/b=0.1$, $c_x/a=0.75$, $\alpha=30^\circ$) and (e) nodal patterns and $\omega(b^2/h)\sqrt{\rho/E}$ for FFFF homogeneous cracked square parallelepipeds modeled as classically-thin cracked plates (Huang and Leissa [2]) ($\hat{m}=0$, $d/b=0.2,0.5$, $h/b=0.01$, $c_y/b=0.5,0.75$, $\alpha=0^\circ$, 30°).

face conditions modeled as plates with various thickness ratios (h/a) and having side cracks at various locations (c_x/a and c_y/b), inclination angles (α), and length ratios (d/a and d/b). Three types of conditions on side faces 1,2,3,4 (see Fig. 1) are considered, namely SSSS, FFFF and CFCF, where S, F and C denote simply-supported, free, and clamped face conditions, respectively. The SSSS rectangular parallelepipeds are assumed simply-supported on the faces $x=0$, $x=a$, $y=0$, and $y=b$. The corresponding geometric face conditions are $U_c=U_3=0$ at $x=0$ and $x=a$, and $U_1=U_3=0$ at $y=0$ and $y=b$. Thus, in Eq. (9), $g_1(x, y, z)=y(b-y)$, $g_2(x, y, z)=x(a-x)$, and $g_3(x, y, z)=x(a-x)y(b-y)$. The FFFF rectangular parallelepipeds are assumed stress free on the faces

d

c_x/a	α	d/b	Mode Number 1	2	3	4	5
0.75	30°	0.2	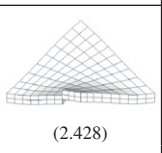 (2.428)	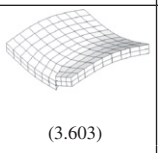 (3.603)	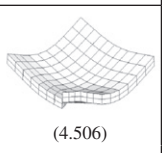 (4.506)	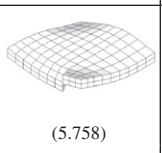 (5.758)	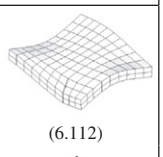 (6.112)
				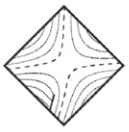	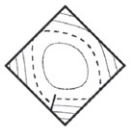		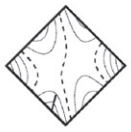
		0.5	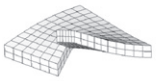 (1.722)	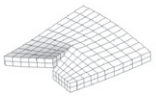 (2.471)	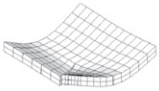 (4.169)	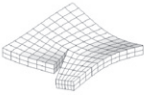 (4.497)	* 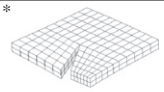 (4.986)
				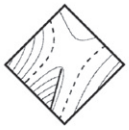	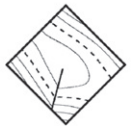	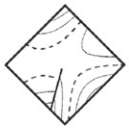	

e

α	c/b	d/a	Mode Number 1	2	3	4	5
		0	 (4.076)	 (5.934)	 (7.348)	 (10.54)	 (10.54)
0°	0.5	0.2	 (3.849)	 (5.698)	 (7.127)	 (9.705)	 (10.03)
		0.5	 (2.496)	 (4.470)	 (6.649)	 (6.990)	 (9.654)
	0.75	0.2	 (3.925)	 (5.825)	 (7.223)	 (9.563)	 (10.38)
		0.5	 (2.615)	 (4.630)	 (6.385)	 (7.584)	 (10.06)
30°	0.75	0.2	 (3.946)	 (5.768)	 (7.223)	 (9.772)	 (10.30)
		0.5	 (2.840)	 (4.113)	 (6.712)	 (7.520)	 (9.793)

Fig. 4. (*continued*)

$x=0$, $x=a$, $y=0$, and $y=b$. Thus, in Eq. (9), $g_1(x, y, z)=g_2(x, y, z)=g_3(x, y, z)=1$. The CFCF rectangular parallelepipeds are assumed clamped on the faces $x=0$ and $x=a$, and stress free on the faces $y=0$ and $y=b$. The corresponding clamped face conditions are $U_1=U_2=U_3=0$ at $x=0$, and $U_1=U_2=U_3=0$ at $x=a$. Thus, in Eq. (9), $g_1(x, y, z)=1$, $g_2(x, y, z)=g_3(x, y, z)=x(a-x)$. As stated earlier, imbedded inside the adopted Gram–Schmidt orthogonalization procedure in Eq. (7) are associated face functions in which $P_j^{(i)}(x)$ satisfy the above SSSS, FFFF, and CFCF face conditions for U_i on the parallelepiped faces, $x=0$ and $x=a$, while $Q_k^{(i)}(y)$ satisfy the

a

α	c_x/a	d/b	Mode Number 1	2	3	4	5
90°	0.25	0.2	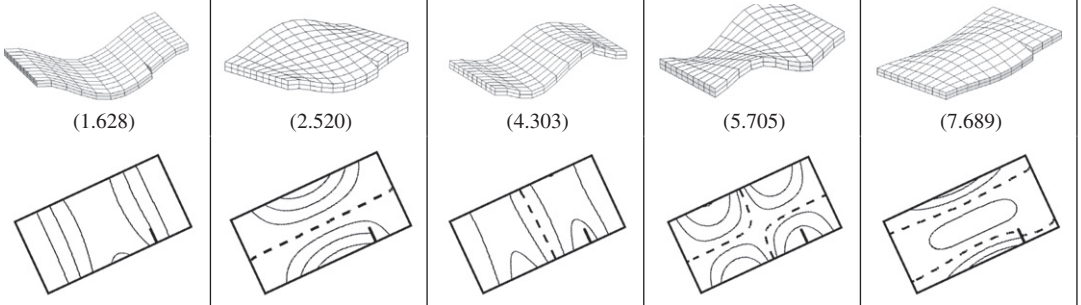 (1.628)	(2.520)	(4.303)	(5.705)	(7.689)
		0.5	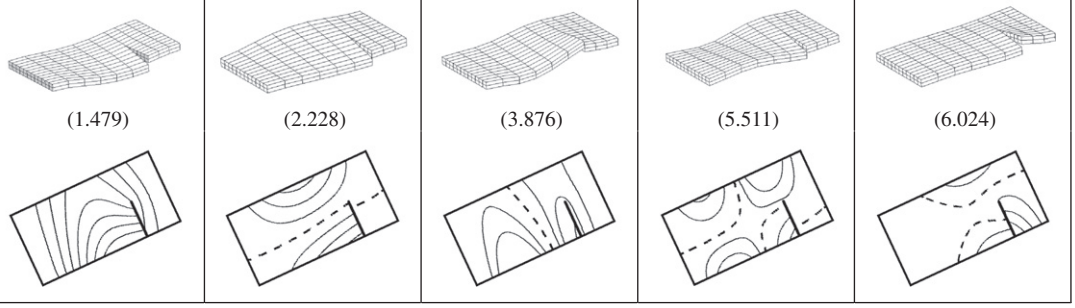 (1.479)	(2.228)	(3.876)	(5.511)	(6.024)

b

α	c_x/a	d/b	Mode Number 1	2	3	4	5
90°	0.5	0.2	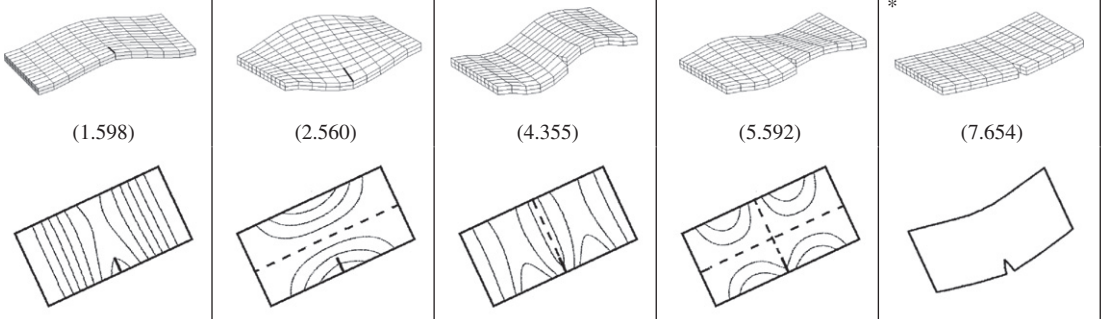 (1.598)	(2.560)	(4.355)	(5.592)	* (7.654)
		0.5	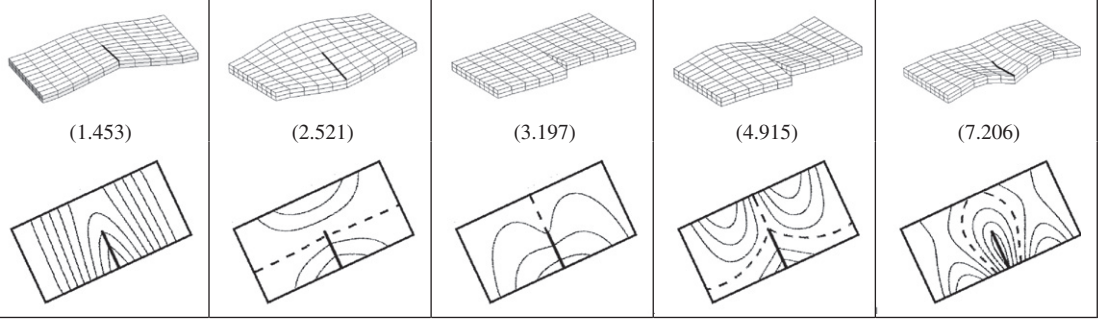 (1.453)	(2.521)	(3.197)	(4.915)	(7.206)

Fig. 5. (a) Mode shapes, nodal patterns and $\omega(b^2/h)\sqrt{\rho/E}$ for CFCF homogeneous cracked rectangular parallelepipeds modeled as moderately thick cracked plates ($\hat{m}=0$, $a/b=2$, $d/b=0.2,0.5$, $h/b=0.1$, $c_x/a=0.25$, $\alpha=90^\circ$); (b) mode shapes, nodal patterns and $\omega(b^2/h)\sqrt{\rho/E}$ for CFCF homogeneous cracked rectangular parallelepipeds modeled as moderately thick cracked plates ($\hat{m}=0$, a/b=2, $d/b=0.2,0.5$, $h/b=0.1$, $c_x/a=0.5$, $\alpha=90^\circ$); (c) mode shapes, nodal patterns and $\omega(b^2/h)\sqrt{\rho/E}$ for CFCF homogeneous cracked rectangular parallelepipeds modeled as moderately thick cracked plates ($\hat{m}=0$, a/b=2, $d/b=0.2,0.5$, $h/b=0.1$, $c_x/a=0.25$, $\alpha=135^\circ$) and (d) mode shapes, nodal patterns and $\omega(b^2/h)\sqrt{\rho/E}$ for CFCF homogeneous cracked rectangular parallelepipeds modeled as moderately thick cracked plates ($\hat{m}=0$, a/b=2, $d/b=0.2,0.5$, $h/b=0.1$, $c_x/a=0.5$, $\alpha=135^\circ$).

SSSS, FFFF, and CFCF face conditions for U_i on the parallelepiped faces, $y=0$ and $y=b$. Poisson's ratio (ν) is set equal to 0.3 for the homogeneous parallelepipeds analyzed.

The results for cracked plates were obtained using orthogonal polynomial solution size, $\hat{N}_x \times \hat{N}_y = 9 \times 9$ (Eq. (7)), crack functions, $\hat{N}_c = 6$ (Eq. (9)), and algebraic polynomial solution size (Eq. (7)), $\hat{N}_z = 4$ (for h/b less than 0.05) and 6, taking on correspondingly cubic-order and 5th-order transverse shear deformation through the parallelepiped thickness (yielding a 1620-term solution matrix size).

c

α	c_x/a	d/b	Mode Number 1	2	3	4	5
135°	0.25	0.2	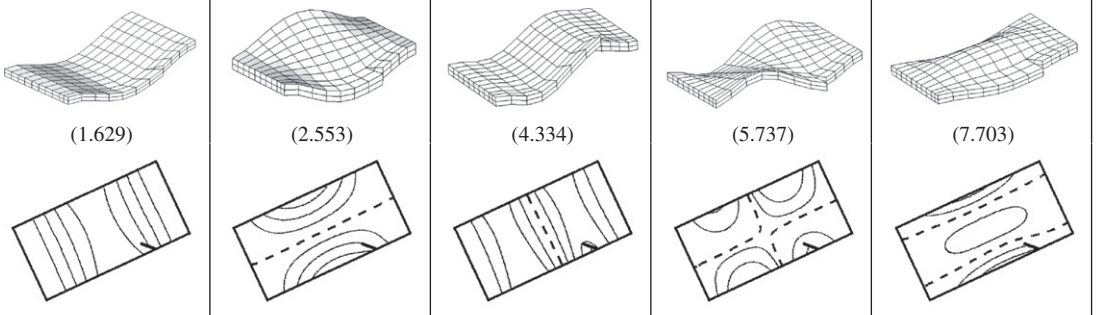 (1.629)	(2.553)	(4.334)	(5.737)	(7.703)
		0.5	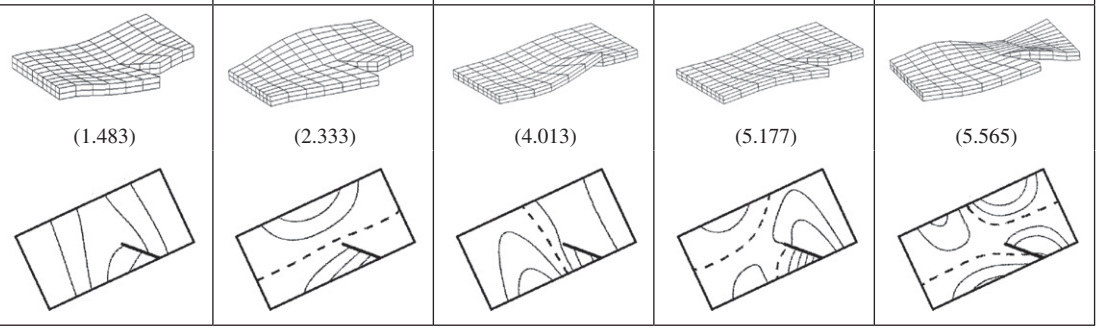 (1.483)	(2.333)	(4.013)	(5.177)	(5.565)

d

α	c_x/a	d/b	Mode Number 1	2	3	4	5
135°	0.5	0.2	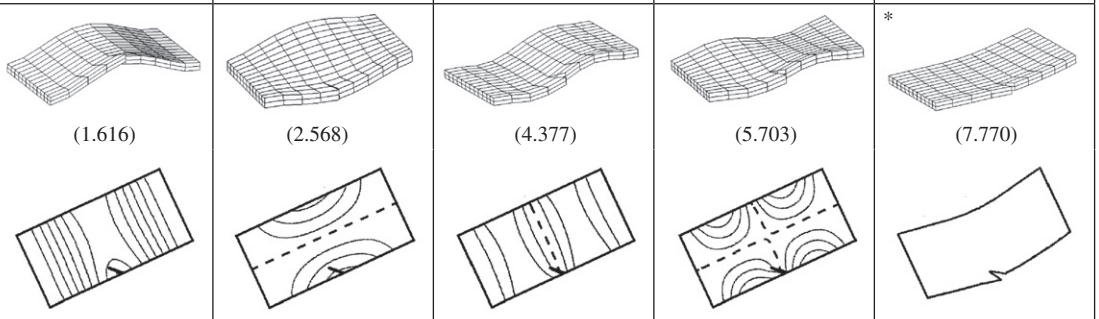 (1.616)	(2.568)	(4.377)	(5.703)	* (7.770)
		0.5	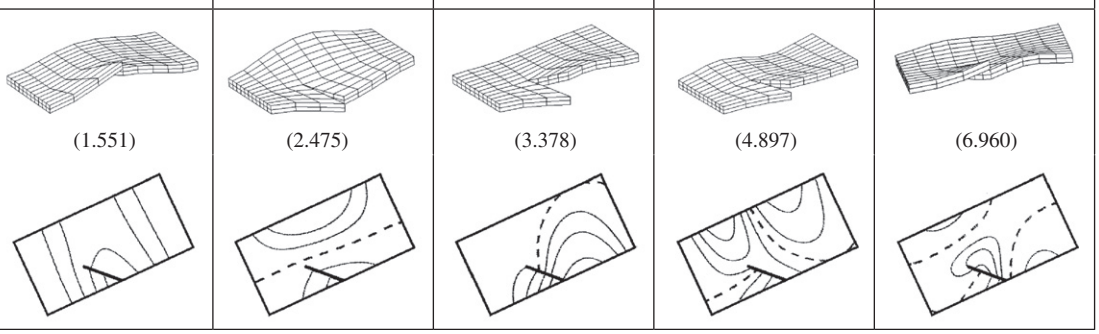 (1.551)	(2.475)	(3.378)	(4.897)	(6.960)

Fig. 5. (*continued*)

Tables 5 and 6 show the first five non-dimensional frequency parameters for SSSS square Al/Al_2O_3 FGM parallelepipeds modeled as moderately thick ($h/b=0.1$) and thick ($h/b=0.2$) plates having horizontal side cracks ($\alpha=0^\circ$) with various length ratios (d/b) positioned at $c_y/b=0.5$. Comparisons of $\omega(b^2/h)\sqrt{\rho_c/E_c}$ 3-D solutions exact to at least three significant figures using an orthogonal polynomial solution size $\hat{N}_x \times \hat{N}_y = 11 \times 11$ (Eq. (7)), and algebraic polynomial solutions size (Eq. (7)), $\hat{N}_z = 6$, for intact SSSS parallelepipeds having no cracks (i.e., $d/a=0$) with previously published solutions by Mac and Huan [19] and He et al. [21] are also shown in Table 5. Mac and Huang [19] employed a first-order shear deformation plate theory and He et al. [21] utilized a higher-order plate theory. The present 3-D elasticity-based $\omega(b^2/h)\sqrt{\rho_c/E_c}$ upper bounds on the exact solutions agree favorably with the $\omega(b^2/h)\sqrt{\rho_c/E_c}$ higher-order shear deformable plate solutions of He et al. [21] up to three or four significant figures. Yet, the present 3-D $\omega(b^2/h)\sqrt{\rho_c/E_c}$ upper bounds on the exact solutions are slightly larger than the $\omega(b^2/h)\sqrt{\rho_c/E_c}$ solutions of Mac and Huang [19], mainly due to the full transverse shear flexibilities inherent to the present 3-D

a

α	c_x/a	d/b	Mode Number 1	2	3	4	5
90°	0.25	0.2	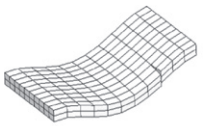 (1.525) 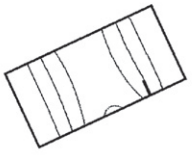	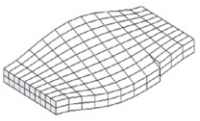 (2.353) 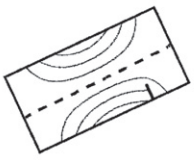	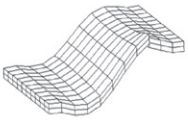 (4.016) 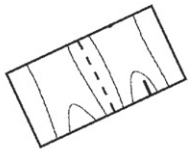	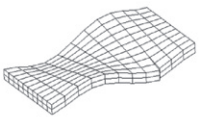 (5.314) 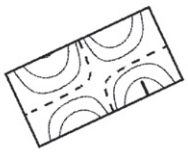	* 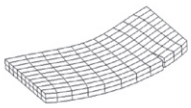 (7.139) 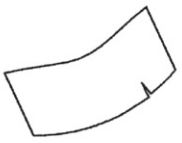
		0.5	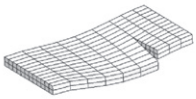 (1.383) 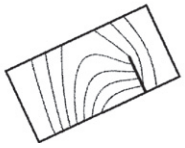	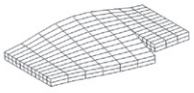 (2.082) 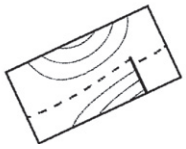	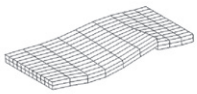 (3.618) 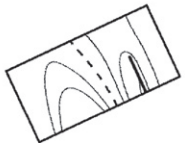	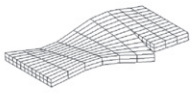 (5.136) 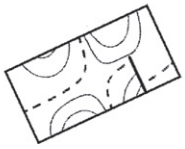	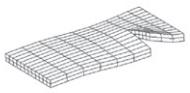 (5.601) 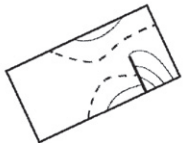

b

α	c_x/a	d/b	Mode Number 1	2	3	4	5
90°	0.5	0.2	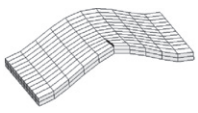 (1.497) 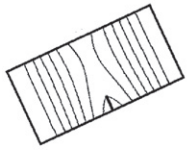	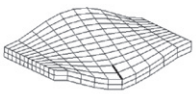 (2.391) 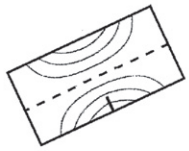	 (4.064) 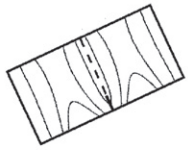	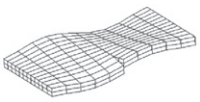 (5.207) 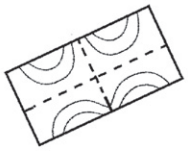	* 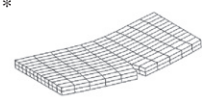 (6.914) 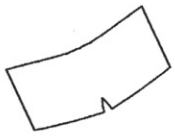
		0.5	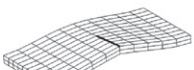 (1.361) 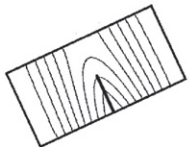	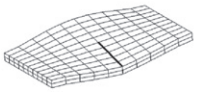 (2.355) 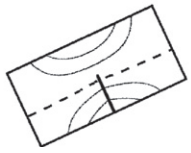	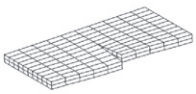 (2.977) 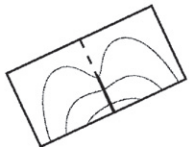	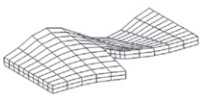 (4.585) 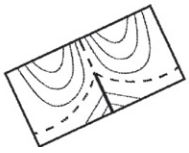	* 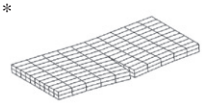 (6.592) 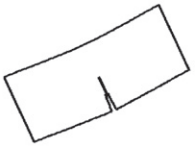

Fig. 6. (a) Mode shapes, nodal patterns and $\omega(b^2/h)\sqrt{\rho_c/E_c}$ for CFCF cracked rectangular Al/ ZrO_2 FGM parallelepipeds modeled as moderately thick cracked Al/ ZrO_2 FGM plates ($\hat{m}=5$, a/b=2, $d/b=0.2,0.5$, $h/b=0.1$, $c_x/a=0.5$, $\alpha=90^\circ$); (b) mode shapes, nodal patterns and $\omega(b^2/h)\sqrt{\rho_c/E_c}$ for CFCF cracked rectangular Al/ ZrO_2 FGM parallelepipeds modeled as moderately thick cracked Al/ ZrO_2 FGM plates ($\hat{m}=5$, a/b=2, $d/b=0.2,0.5$, $h/b=0.1$, $c_x/a=0.5$, $\alpha=90^\circ$); (c) mode shapes, nodal patterns and $\omega(b^2/h)\sqrt{\rho_c/E_c}$ for CFCF cracked rectangular Al/ ZrO_2 FGM parallelepipeds modeled as moderately thick cracked Al/ ZrO_2 FGM plates ($\hat{m}=5$, a/b=2, $d/b=0.2,0.5$, $h/b=0.1$, $c_x/a=0.25$, $\alpha=135^\circ$) and (d) mode shapes, nodal patterns and $\omega(b^2/h)\sqrt{\rho_c/E_c}$ for CFCF cracked rectangular Al/ ZrO_2 FGM parallelepipeds modeled as moderately thick cracked Al/ ZrO_2 FGM plates ($\hat{m}=5$, a/b=2, $d/b=0.2,0.5$, $h/b=0.1$, $c_x/a=0.5$, $\alpha=135^\circ$).

elasticity-based Ritz formulation (showing analogous trends observed and previously discussed in Table 4).

Generally speaking, $\omega(b^2/h)\sqrt{\rho_c/E_c}$ decrease with increasing $\hat{m}$—the volume fraction parameter that governs the material variation profile in the thickness direction (see Eq. (1)). Decreasing $\omega(b^2/h)\sqrt{\rho_c/E_c}$ with increasing $\hat{m}$ is not only because increasing $\hat{m}$ reduces the stiffness more than it does the mass of plate, but also because $\omega(b^2/h)\sqrt{\rho_c/E_c}$ decreases with increasing

c

α	c_x/a	d/b	Mode Number 1	2	3	4	5
135°	0.25	0.2	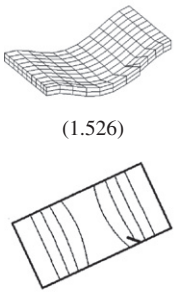 (1.526)	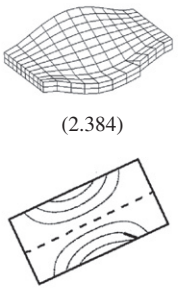 (2.384)	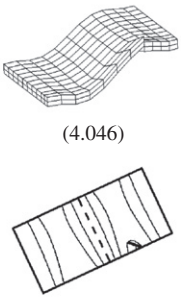 (4.046)	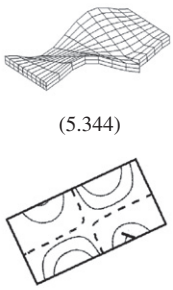 (5.344)	* 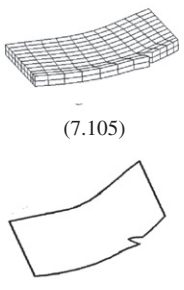 (7.105)
		0.5	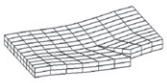 (1.388)	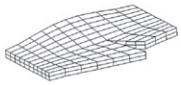 (2.179)	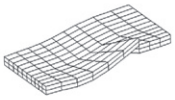 (3.748)	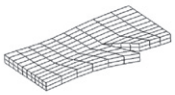 (4.817)	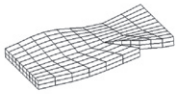 (5.181)
			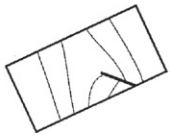	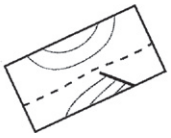	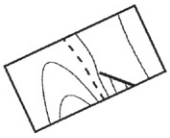	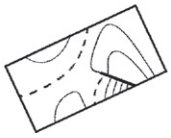	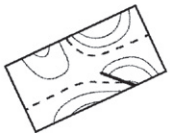

d

α	c_x/a	d/b	Mode Number 1	2	3	4	5
135°	0.5	0.2	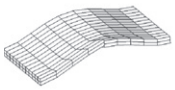 (1.514)	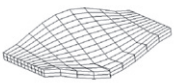 (2.399)	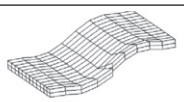 (4.086)	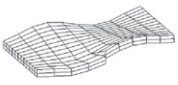 (5.310)	* 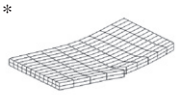 (7.019)
			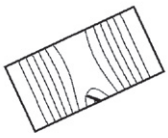	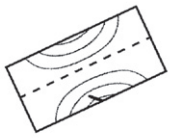	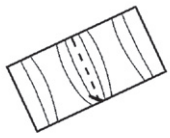	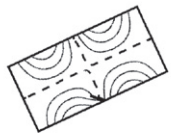	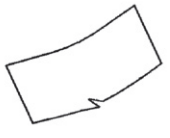
		0.5	 (1.453)	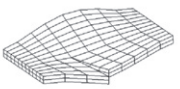 (2.312)	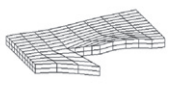 (3.148)	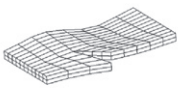 (4.563)	 (6.479)
			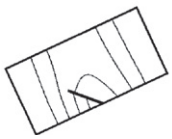	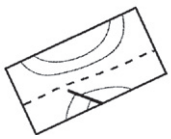	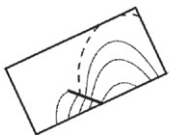	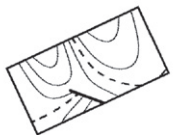	

Fig. 6. (*continued*)

parallelepiped thickness (h). As the crack length ratio (d/a) increases, $\omega(b^2/h)\sqrt{\rho_c/E_c}$ decrease, due to the reduction in the parallelepiped stiffness. There is no clear trend between the reduction of $\omega(b^2/h)\sqrt{\rho_c/E_c}$ for SSSS parallelepipeds due to a crack and the value of $\hat{m}$. However, two extremes in $\omega(b^2/h)\sqrt{\rho_c/E_c}$ trends can be seen across the wide spectrum of SSSS cracked FGM parallelepiped data reported in Tables 5 and 6. A shallow crack of length ratio, $d/a=0.1$, only reduce the first five $\omega(b^2/h)\sqrt{\rho_c/E_c}$ less than 2% relative to those for an intact SSSS parallelepiped ($d/a=0$). In contrast, a deep crack of length ratio, $d/a=0.5$, decreases up to 18% the second mode $\omega(b^2/h)\sqrt{\rho_c/E_c}$ of the SSSS FGM ($\hat{m}=10$) parallelepiped modeled as moderately thick plate ($h/b=0.1$).

Tables 7 and 8 list the first five nonzero $\omega(b^2/h)\sqrt{\rho_c/E_c}$ for completely free (FFFF) square FGM parallelepipeds modeled as thin ($h/b=0.02$) and moderately thick ($h/b=0.1$) plates. The FGM parallelepipeds are assumed aluminum (Al) and alumina (Al_2O_3), and the material properties vary as Eq. (1) with $\hat{m}=5$ along the thickness direction. The effects of crack length ratios (d/a), crack positions (c_x/a and c_y/b), and crack inclination angles (α) on $\omega(b^2/h)\sqrt{\rho_c/E_c}$ are studied. Not listed are the rigid body vibration modes (zero $\omega(b^2/h)\sqrt{\rho_c/E_c}$) for the FFFF parallelepipeds examined. Similar to the findings of Tables 5 and 6, the $\omega(b^2/h)\sqrt{\rho_c/E_c}$ in Tables 7 and 8 decrease with increasing FFFF FGM parallelepiped thickness and crack length (d/a). When the location of crack changes from $c_y/b=0.5$ to 0.75, $\omega(b^2/h)\sqrt{\rho_c/E_c}$ generally increases

Table 4
Comparisons of $\omega(b^2/h)\sqrt{\rho/E}$ predicted by various theories for homogeneous cracked, SSSS square parallelepipeds modeled as square, thin to moderately thick SSSS plates (h/b=0.002, 0.05,0.1) with horizontal side cracks (α=0°) having various length ratios (d/a) and positioned at c_y/b=0.5[a].

d/a	h/b	Mode				
		1	2	3	4	5
0.2	0.002	[5.961]	[14.89]	[14.93]	[23.84]	[29.62]
		(5.961)	(14.89)	(14.92)	(23.84)	(29.62)
		{5.961}	{14.88}	{14.93}	{23.84}	{29.62}
	0.05	[5.961]	[14.89]	[14.93]	[23.84]	[29.62]
		(5.900)	(14.54)	(14.55)	(22.91)	(28.29)
		{5.905}	{14.56}	{14.57}	{22.95}	{28.35}
	0.1	[5.961]	[14.89]	[14.93]	[23.84]	[29.62]
		(5.750)	(13.66)	(13.69)	(20.87)	(25.41)
		{5.758}	{13.72}	{13.74}	{20.99}	{25.57}
0.4	0.002	[5.810]	[14.46]	[14.60]	[21.57]	[27.91]
		(5.810)	(14.46)	(14.60)	(21.56)	(27.91)
		{5.810}	{14.47}	{14.60}	{21.57}	{27.91}
	0.05	[5.810]	[14.46]	[14.60]	[21.57]	[27.91]
		(5.725)	(13.90)	(14.23)	(20.48)	(26.49)
		{5.730}	{13.92}	{14.25}	{20.54}	{26.55}
	0.1	[5.810]	[14.46]	[14.60]	[21.57]	[27.91]
		(5.562)	(12.84)	(13.39)	(18.54)	(23.83)
		{5.572}	{12.90}	{13.43}	{18.66}	{23.97}

[a] [ ]: classical thin plate theory [2,3]; ( ): Mindlin plate theory [4]; { }: present 3-D elasticity-based solution.

Table 5
Frequency parameters $\omega(b^2/h)\sqrt{\rho_C/E_C}$ for Al/Al_2O_3 FGM ($\hat{m}$ = 0,1,5,10) SSSS square parallelepipeds modeled as Al/Al_2O_3 FGM SSSS square, moderately thick plates (h/b=0.1) with horizontal side cracks (α=0°) having various length ratios (d/a) and positioned at c_Y/b = 0.5[a].

$\hat{m}$	d/a	Mode				
		1	2	3	4	5
0	0	5.777	13.81	13.81	19.48	19.48
	0.1	5.775	13.78	13.80	19.25	19.48
	0.2	5.758	13.72	13.74	18.57	19.48
	0.3	5.697	13.54	13.60	17.64	19.48
	0.4	5.572	12.90	13.43	16.79	18.66
	0.5	5.385	11.40	13.35	16.19	17.35
1	0	4.426 (4.347) [4.426]	10.63 (10.42)	10.63 (10.42)	16.20 (15.94)	16.20
	0.1	4.425	10.60	10.62	16.01	16.20
	0.2	4.411	10.56	10.58	15.44	16.20
	0.3	4.365	10.43	10.46	14.67	15.74
	0.4	4.270	9.963	10.34	13.95	14.45
	0.5	4.127	8.819	10.28	13.34	13.51
5	0	3.772	8.927	8.927	12.64	12.64
	0.1	3.771	8.908	8.924	12.49	12.64
	0.2	3.759	8.867	8.885	12.05	12.64
	0.3	3.719	8.743	8.791	11.45	12.64
	0.4	3.636	8.316	8.687	10.89	11.97
	0.5	3.513	7.334	8.635	10.49	11.18
10	0	3.641 (3.592) [3.642]	8.587 (8.504)	8.587 (8.504)	11.52 (12.89)	11.52
	0.1	3.640	8.567	8.583	11.39	11.52
	0.2	3.629	8.526	8.546	10.98	11.52
	0.3	3.590	8.401	8.456	10.44	11.52
	0.4	3.510	7.977	8.356	9.929	11.47
	0.5	3.391	7.025	8.307	9.573	10.73

[a] ( ): Mac and Huang [19]; [ ]: He et al. [21]

overall, especially for the first mode. When the inclination angle of crack varies from α=0° to 30°, and then to α=45°, $\omega(b^2/h)\sqrt{\rho_c/E_c}$ in the fundamental mode increases, reflecting a significant increase

Table 6
Frequency parameters $\omega(b^2/h)\sqrt{\rho_C/E_C}$ for Al/Al_2O_3 FGM ($\hat{m}$ = 0,1,5,10)) SSSS square parallelepipeds modeled as Al/Al_2O_3 FGM SSSS square, thick plates (h/b=0.2) with horizontal side cracks (α=0°) having various length ratios (d/a) and positioned at c_Y/b = 0.5

$\hat{m}$	d/a	Mode				
		1	2	3	4	5
0	0	5.304	9.742	9.742	11.65	11.65
	0.1	5.302	9.627	9.742	11.62	11.64
	0.2	5.285	9.289	9.742	11.54	11.59
	0.3	5.225	8.827	9.742	11.30	11.47
	0.4	5.104	8.397	9.742	10.58	11.33
	0.5	4.927	8.095	9.228	9.742	11.27
1	0	4.099	8.089	8.089	9.107	9.107
	0.1	4.098	7.994	8.089	9.084	9.103
	0.2	4.084	7.713	8.089	9.027	9.063
	0.3	4.038	7.330	8.089	8.854	8.961
	0.4	3.944	6.972	8.089	8.309	8.848
	0.5	3.805	6.715	7.265	8.089	8.788
5	0	3.405	6.296	6.296	7.343	7.343
	0.1	3.404	6.222	6.296	7.325	7.341
	0.2	3.393	6.005	6.296	7.276	7.310
	0.3	3.355	5.708	6.296	7.123	7.232
	0.4	3.277	5.430	6.296	6.652	7.144
	0.5	3.163	5.227	5.811	6.296	7.082
10	0	3.264	5.749	5.749	6.975	6.975
	0.1	3.263	5.682	5.749	6.958	6.973
	0.2	3.253	5.483	5.749	6.910	6.945
	0.3	3.217	5.211	5.749	6.759	6.874
	0.4	3.143	4.957	5.749	6.298	6.794
	0.5	3.035	4.776	5.494	5.749	6.689

of stiffness in the fundamental mode of FFFF cracked FGM parallelepipeds. Two extremes in $\omega(b^2/h)\sqrt{\rho_c/E_c}$ trends can also be seen across the spectrum of FFFF cracked FGM parallelepiped data reported in Tables 7 and 8. A shallow crack with d/a=0.1 only reduces the frequencies less than 3% relative to those for an intact FFFF parallelepiped (d/a=0), whereas a deep crack with length ratio, d/a=0.5, decreases $\omega(b^2/h)\sqrt{\rho_c/E_c}$ up to 43%, occurring at the fourth mode of FFFF FGM ($\hat{m}$ = 10) parallelepiped having a crack positioned at c_y/b=0.5 and crack inclination α=45° (Table 8).

Tables 9 and 10 summarize the first five $\omega(b^2/h)\sqrt{\rho_c/E_c}$ for CFCF cracked FGM rectangular parallelepipeds (a/b=2) modeled as moderately thick (h/b=0.1) and very thick (h/b=0.3) plates. The parallelepipeds are assumed made of aluminum (Al) and zirconia (ZrO_2), the material properties varying through the parallelepiped thickness according to Eq. (1) with $\hat{m}$=1, 5 and 10. The crack configuration under consideration is similar to that shown in Fig. 1b. Table 9 reveals that $\omega(b^2/h)\sqrt{\rho_c/E_c}$ of Al/ZrO_2 FGM parallelepipeds modeled as moderately plates (h/b=0.1) increase as volume fraction $G(z)=\frac{E(z)}{[2(1+\nu(z)]}$=1 increases to $\hat{m}$ = 5, and $\omega(b^2/h)\sqrt{\rho_c/E_c}$ decrease as $\hat{m}$ = 5 further increases to $\hat{m}$ = 10. Table 10 shows that $\omega(b^2/h)\sqrt{\rho_c/E_c}$ of Al/ZrO_2 FGM parallelepipeds modeled as very thick plates (h/b=0.3) decrease with increasing $\hat{m}$, and the trend is consistent to that seen in Tables 5 and 6 for SSSS square Al/Al_2O_3 FGM parallelepipeds modeled as thick plates. There are less clear trends on changes in $\omega(b^2/h)\sqrt{\rho_c/E_c}$ caused by shifting the crack position from c_x/a=0.25 to 0.5 or by changing inclination angle of crack α from 90° to 135°. Tables 9 and 10 indicate that a shallow crack with d/b=0.1 results in maximum reduction in $\omega(b^2/h)\sqrt{\rho_c/E_c}$ about 5% relative to $\omega(b^2/h)\sqrt{\rho_c/E_c}$ for an intact plate, which occurs at the third mode of the plate with $\hat{m}$ = 5 and having a crack with c_x/a=0.25 and α=90° in Table 9. A large crack with d/b=0.5 decreases the frequencies up to 29%, occurring at the fifth mode of the plate with $\hat{m}$ = 5 and having a deep crack (c_x/a=0.5) and crack orientation α=90° in Table 10.

Table 7
Frequency parameters $\omega(b^2/h)\sqrt{\rho_C/E_C}$ for Al/Al_2O_3 FGM ($\hat{m}=5$) FFFF square parallelepipeds modeled as Al/Al_2O_3 FGM FFFF square, thin plates ($h/b=0.02$) with various positioned (c_y/b) and inclined (α) side cracks with varying length ratios (d/a).

α	$\hat{m}$	c_y/b	d/a	Mode				
				1	2	3	4	5
0°			0	2.665	3.896	4.824	6.881	6.881
			0.1	2.631	3.853	4.779	6.738	6.752
	5	0.5	0.2	2.514	3.726	4.668	6.332	6.516
			0.3	2.287	3.506	4.538	5.614	6.366
			0.4	1.963	3.210	4.431	4.947	6.299
			0.5	1.627	2.896	4.361	4.536	6.292
	5		0.1	2.641	3.880	4.808	6.750	6.837
			0.2	2.563	3.819	4.737	6.228	6.764
		0.75	0.3	2.392	3.644	4.521	5.479	6.684
			0.4	2.082	3.304	4.280	5.127	6.613
			0.5	1.703	3.009	4.188	4.955	6.549
30°	5		0.1	2.638	3.862	4.789	6.761	6.779
			0.2	2.551	3.764	4.705	6.440	6.553
		0.5	0.3	2.376	3.600	4.578	5.718	6.348
			0.4	2.080	3.369	4.325	4.971	6.176
			0.5	1.710	3.157	3.952	4.681	6.069
	5		0.1	2.642	3.877	4.807	6.772	6.829
			0.2	2.575	3.781	4.737	6.364	6.710
		0.75	0.3	2.437	3.494	4.608	5.702	6.560
			0.4	2.189	3.028	4.490	5.196	6.439
			0.5	1.847	2.662	4.394	4.900	6.383
45°	5	0.5	0.1	2.645	3.871	4.799	6.787	6.806
			0.2	2.584	3.759	4.721	6.495	6.575
			0.3	2.470	3.683	4.652	5.905	6.387
			0.4	2.202	3.520	4.253	5.023	6.113
			0.5	1.865	3.271	3.860	4.692	5.889
	5	0.75	0.1	2.649	3.881	4.811	6.803	6.839
			0.2	2.600	3.824	4.772	6.543	6.742
			0.3	2.502	3.533	4.651	5.891	6.546
			0.4	2.326	3.084	4.543	5.303	6.377
			0.5	2.015	2.670	4.402	4.925	6.252

Table 8
Frequency parameters $\omega(b^2/h)\sqrt{\rho_C/E_C}$ for Al/Al_2O_3 FGM ($\hat{m}=5$) FFFF square parallelepipeds modeled as Al/Al_2O_3 FGM FFFF square, moderately thick plates ($h/b=0.1$) with various positioned (c_y/b) and inclined (α) side cracks with varying length ratios (d/a).

α	$\hat{m}$	c_y/b	d/a	Mode				
				1	2	3	4	5
0°			0	2.512	3.746	4.608	6.270	6.270
			0.1	2.484	3.690	4.552	6.125	6.168
	5	0.5	0.2	2.369	3.536	4.431	5.760	5.918
			0.3	2.146	3.285	4.307	5.058	5.800
			0.4	1.839	2.978	4.217	4.455	5.601
			0.5	1.525	2.666	4.085	4.149	4.212
	5		0.1	2.494	3.723	4.586	6.147	6.230
			0.2	2.420	3.639	4.488	5.642	6.149
		0.75	0.3	2.252	3.404	4.242	5.055	6.057
			0.4	1.952	3.040	4.051	4.760	5.031
			0.5	1.593	2.769	3.655	3.987	4.622
30°	5		0.1	2.490	3.703	4.565	6.150	6.190
			0.2	2.403	3.587	4.468	5.849	5.951
		0.5	0.3	2.228	3.400	4.321	5.138	5.772
			0.4	2.078	3.160	4.107	4.589	5.583
			0.5	1.605	2.885	3.573	3.661	4.340
	5		0.1	2.495	3.722	4.588	6.170	6.227
			0.2	2.428	3.603	4.506	5.758	6.112
		0.75	0.3	2.288	3.271	4.372	5.178	5.977
			0.4	2.046	2.816	4.270	4.762	5.881
			0.5	1.722	2.471	4.169	4.497	4.986
45°	5	0.5	0.1	2.496	3.715	4.578	6.180	6.123
			0.2	2.437	3.636	4.511	5.958	6.008
			0.3	2.318	3.503	4.387	5.277	5.794
			0.4	2.108	3.309	4.021	4.613	5.091
			0.5	1.717	2.710	3.010	3.552	4.323
	5	0.75	0.1	2.499	3.727	4.593	6.197	6.235
			0.2	2.452	3.630	4.531	5.898	6.127
			0.3	2.349	3.327	4.422	5.313	5.973
			0.4	2.170	2.860	4.312	4.821	5.831
			0.5	1.869	2.483	4.150	4.528	5.192

5. Vibration modes of cracked FGM parallelepipeds

Depicted in Figs. 2–6 are 3-D mode shapes and nodal patterns and $\omega(b^2/h)\sqrt{\rho/E}$ (for homogeneous) and $\omega(b^2/h)\sqrt{\rho_c/E_c}$ (for FGM) SSSS, FFFF, and CFCF parallelepipeds modeled as moderately thick plates ($h/b=0.1$). The influence of volume fraction ($\hat{m}$), crack length ratios (d/a and d/b), crack positions (c_x/a and c_y/b), and crack inclination angles (α) on the 3-D mode shapes and nodal patterns are studied. No published vibration modes shapes using 3-D approaches for cracked homogeneous and FGM parallelepipeds having SSSS, FFFF, and CFCF face conditions are known to exist.

For cracked parallelepipeds shear deformation and rotary inertia effects are significant in the lower predominately flexural modes and substantially in the higher ones, while large elastic warping stresses considerably increase the predominately torsional modes. Vibratory stresses become unbounded near the crack terminus edge, showing a well-known fracture mechanics fact that the order of 3-D components of stresses are $\sigma_{ij} \sim O(r^{-1/2})$ (see Appendix), as r approaches zero (see Fig. 1). Nonetheless, these unbounded stresses oftentimes lead to theoretical prediction errors in the lower modes as well as some of the higher modes of cracked rectangular parallelepipeds.

In the present 3-D continuum formulation, complicating effects, such as shear deformation, rotary inertia, and elastic warping stresses at the clamped faces of the CFCF parallelepiped mode shapes depicted in Figs. 5–6, are inherent. Most of all, the key advantage of the present 3-D continuum analysis is that no kinematic constraints (as in beam, plate or shell theories) are dictated, except those enforced through the assumed face functions defined at the top of the previous Section 4.

All possible 3-D vibratory displacement patterns falling within the first five modes are depicted and appropriately described in captions of Figs. 2–6. For an intact homogeneous parallelepiped, longitudinal flexure, sideways flexure, longitudinal extension, and torsional modes (even dilatational modes) are each uncoupled, forming four distinct symmetry classes of vibratory motion. For cracked FGM parallelepipeds, depending on the volume fraction ($\hat{m}$), crack length ratios (d/a and d/b), crack positions (c_x/a and c_y/b), and crack inclination angles (α), distinct symmetry classes of modes may be possible with longitudinal flexure and torsional modes classified into one symmetry class, and sideways flexure and longitudinal extensional modes classified into a second symmetry class. Generally speaking, for $\hat{m} \neq 0$, $d/a \neq 0$, $d/b \neq 0$, $c_x/a \neq 0$, and $c_y/b \neq 0$, and $\alpha \neq 0°$, all possible modes are inseparably coupled with no identifiable symmetry classes present.

The dynamic stress field near the crack terminus edge within a FGM parallelepiped may be classified as three basic dynamic responses each associated with a local mode of crack deformation. First, a crack opening mode in FGM parallelepiped vibration is associated with local displacement in which the crack surfaces move directly apart; second, a crack shearing or edge-sliding mode in FGM parallelepiped vibration is characterized by deformations in which the crack surfaces slide over one another perpendicular to the leading terminus edge of the crack; third, a crack tearing mode in FGM parallelepiped vibration finds the

Table 9

Frequency parameters $\omega(b^2/h)\sqrt{\rho_c/E_c}$ for Al/ ZrO_2 FGM CFCF rectangular ($a/b=2$) parallelepipeds modeled as Al/ZrO_2 FGM ($\hat{m}=1$) CFCF rectangular, moderately thick plates ($h/b=0.1$) with various positioned (c_x/a) and inclined (α) side cracks with varying length ratios (d/b)

α	$\hat{m}$	c_x/a	d/b	Mode				
				1	2	3	4	5
90°	1	0.25	0	1.512	2.392	4.083	5.400	7.184
			0.1	1.507	2.374	4.045	5.350	7.164
			0.2	1.499	2.323	3.967	5.265	7.090
			0.3	1.477	2.239	3.851	5.187	6.812
			0.4	1.433	2.140	3.713	5.130	6.158
			0.5	1.362	2.054	3.574	5.084	5.564
	1	0.5	0.1	1.498	2.378	4.067	5.348	7.179
			0.2	1.471	2.359	4.015	5.161	7.176
			0.3	1.433	2.342	3.837	4.848	7.162
			0.4	1.387	2.328	3.434	4.616	6.916
			0.5	1.338	2.323	2.952	4.533	6.652
135°	1	0.25	0.1	1.508	2.381	4.056	5.366	7.170
			0.2	1.500	2.353	3.996	5.293	7.103
			0.3	1.479	2.304	3.901	5.196	6.792
			0.4	1.435	2.233	3.791	5.082	5.870
			0.5	1.365	2.150	3.699	4.780	5.137
	1	0.5	0.1	1.503	2.382	4.071	5.369	7.180
			0.2	1.488	2.367	4.036	5.263	7.166
			0.3	1.469	2.345	3.910	5.031	7.094
			0.4	1.447	2.315	3.595	4.731	6.821
			0.5	1.428	2.281	3.117	4.517	6.425
90°	5	0.25	0	1.539	2.423	4.315	5.450	7.169
			0.1	1.534	2.405	4.096	5.400	7.162
			0.2	1.525	2.353	4.016	5.314	7.139
			0.3	1.502	2.268	3.899	5.237	6.875
			0.4	1.456	2.168	3.759	5.182	6.196
			0.5	1.383	2.082	3.618	5.136	5.601
	5	0.5	0.1	1.524	2.410	4.119	5.398	7.080
			0.2	1.497	2.391	4.064	5.207	6.914
			0.3	1.458	2.373	3.877	4.893	6.761
			0.4	1.411	2.360	3.464	4.666	6.653
			0.5	1.361	2.355	2.977	4.585	6.592
135°	5	0.25	0.1	1.535	2.412	4.107	5.416	7.158
			0.2	1.526	2.384	4.046	5.344	7.105
			0.3	1.505	2.334	3.951	5.247	6.853
			0.4	1.460	2.262	3.841	5.133	5.899
			0.5	1.388	2.179	3.748	4.817	5.181
	5	0.5	0.1	1.529	2.414	4.123	5.419	7.120
			0.2	1.514	2.399	4.086	5.310	7.019
			0.3	1.495	2.376	3.956	5.075	6.924
			0.4	1.473	2.346	3.633	4.775	6.865
			0.5	1.453	2.312	3.148	4.563	6.479
90°	10	0.25	0	1.535	2.416	4.123	5.434	7.027
			0.1	1.530	2.399	4.084	5.383	7.020
			0.2	1.521	2.347	4.004	5.297	6.998
			0.3	1.498	2.262	3.887	5.221	6.853
			0.4	1.452	2.162	3.748	5.166	6.175
			0.5	1.379	2.077	3.608	5.121	5.582
	10	0.5	0.1	1.520	2.403	4.107	5.381	6.940
			0.2	1.493	2.384	4.052	5.191	6.777
			0.3	1.455	2.366	3.865	4.878	6.627
			0.4	1.407	2.353	3.452	4.652	6.521
			0.5	1.358	2.348	2.967	4.572	6.462
135°	10	0.25	0.1	1.531	2.405	4.096	5.400	7.016
			0.2	1.523	2.378	4.035	5.328	6.964
			0.3	1.501	2.328	3.940	5.231	6.831
			0.4	1.456	2.256	3.831	5.118	5.877
			0.5	1.385	2.173	3.738	4.801	5.164
	10	0.5	0.1	1.526	2.407	4.111	5.402	6.978
			0.2	1.511	2.392	4.074	5.294	6.880
			0.3	1.491	2.369	3.945	5.058	6.786
			0.4	1.469	2.340	3.622	4.760	6.730
			0.5	1.450	2.306	3.138	4.550	6.459

Table 10

Frequency parameters $\omega(b^2/h)\sqrt{\rho_c/E_c}$ for Al/ZrO_2 FGM CFCF rectangular ($a/b=2$) parallelepipeds modeled as Al/ZrO_2 FGM ($\hat{m}=10$) CFCF rectangular, very thick plates ($h/b=0.3$) with various positioned (c_x/a) and inclined (α) side cracks with varying length ratios (d/b).

α	$\hat{m}$	c_x/a	d/b	Mode				
				1	2	3	4	5
90°	1	0.25	0	1.348	1.945	2.536	3.268	4.095
			0.1	1.344	1.932	2.534	3.241	4.070
			0.2	1.331	1.892	2.526	3.180	4.021
			0.3	1.301	1.828	2.505	3.091	3.978
			0.4	1.248	1.760	2.460	2.987	3.950
			0.5	1.170	1.707	2.389	2.884	3.924
	1	0.5	0.1	1.336	1.938	2.506	3.253	4.051
			0.2	1.312	1.926	2.448	3.192	3.903
			0.3	1.279	1.914	2.394	3.000	3.701
			0.4	1.241	1.907	2.356	2.653	3.587
			0.5	1.199	1.904	2.300	2.335	3.544
135°	1	0.25	0.1	1.345	1.938	2.533	3.251	4.080
			0.2	1.336	1.916	2.515	3.210	4.041
			0.3	1.314	1.878	2.469	3.148	3.986
			0.4	1.273	1.826	2.394	3.076	3.920
			0.5	1.209	1.769	2.300	3.012	3.602
	1	0.5	0.1	1.341	1.941	2.520	3.258	4.069
			0.2	1.328	1.932	2.484	3.223	3.979
			0.3	1.312	1.918	2.451	3.108	3.804
			0.4	1.293	1.900	2.430	2.837	3.617
			0.5	1.276	1.878	2.424	2.472	3.499
90°	5	0.25	0	1.337	1.906	2.395	3.178	3.970
			0.1	1.333	1.893	2.393	3.153	3.948
			0.2	1.319	1.854	2.386	3.096	3.905
			0.3	1.289	1.793	2.365	3.012	3.865
			0.4	1.234	1.729	2.323	2.915	3.836
			0.5	1.156	1.680	2.256	2.817	3.718
	5	0.5	0.1	1.326	1.900	2.367	3.163	3.926
			0.2	1.303	1.888	2.312	3.102	3.783
			0.3	1.271	1.878	2.261	2.914	3.591
			0.4	1.234	1.871	2.225	2.581	3.483
			0.5	1.194	1.868	2.205	2.243	3.441
135°	5	0.25	0.1	1.334	1.898	2.392	3.162	3.956
			0.2	1.325	1.877	2.375	3.125	3.923
			0.3	1.303	1.841	2.332	3.069	3.873
			0.4	1.262	1.791	2.260	3.003	3.813
			0.5	1.200	1.738	2.172	2.945	3.496
	5	0.5	0.1	1.331	1.902	2.379	3.168	3.943
			0.2	1.318	1.894	2.346	3.133	3.856
			0.3	1.302	1.881	2.315	3.023	3.687
			0.4	1.285	1.865	2.295	2.765	3.508
			0.5	1.268	1.846	2.289	2.418	3.395
90°	10	0.25	0	1.331	1.895	2.347	3.156	3.942
			0.1	1.326	1.882	2.345	3.132	3.921
			0.2	1.313	1.843	2.338	3.075	3.878
			0.3	1.282	1.783	2.318	2.993	3.839
			0.4	1.228	1.719	2.277	2.897	3.800
			0.5	1.150	1.670	2.211	2.800	3.646
	10	0.5	0.1	1.320	1.889	2.319	3.141	3.899
			0.2	1.297	1.878	2.265	3.081	3.757
			0.3	1.266	1.867	2.216	2.893	3.566
			0.4	1.228	1.860	2.180	2.563	3.459
			0.5	1.189	1.858	2.161	2.228	3.418
135°	10	0.25	0.1	1.328	1.887	2.344	3.141	3.929
			0.2	1.318	1.866	2.327	3.104	3.896
			0.3	1.297	1.830	2.285	3.049	3.848
			0.4	1.256	1.781	2.215	2.985	3.788
			0.5	1.194	1.728	2.129	2.927	3.470
	10	0.5	0.1	1.324	1.891	2.332	3.147	3.916
			0.2	1.312	1.883	2.299	3.112	3.829
			0.3	1.296	1.871	2.268	3.003	3.661
			0.4	1.279	1.855	2.249	2.746	3.484
			0.5	1.262	1.835	2.244	2.402	3.372

crack surfaces sliding with respect to one another parallel to the leading terminus edge of the crack. Crack opening and crack shearing or edge-sliding in FGM parallelepiped vibration can be modeled as two-dimensional plane-extension theory of elasticity, classified as symmetric (crack opening) and skew-symmetry (crack shearing/sliding) with respect to the leading edge of the crack. Crack tearing in FGM parallelepiped vibration may be modeled as two-dimensional pure shear (or torsion). Well-known superposition of crack opening, shearing or sliding, and tearing modes or "mixed mode" cracking in FGM parallelepiped vibration is sufficient to describe the most general three-dimensional dynamic aspects of local crack-edge deformation and stress fields in cracked parallelepipeds.

Williams [31] solved the fundamental question of stress field computation near a crack tip in an elastic, isotropic medium using the Airy stress function, as employed in related cracked plate work [35,36] prior to the present 3-D computations. Examining the vibratory actions of a cracked FGM parallelepiped can suggest hypotheses of classical crack propagation [33,34], which states the crack propagates dynamically in the direction perpendicular to the direction of the maximum tensile stress or maximum strain energy release rate in any particular crack opening, crack shearing or sliding, and crack tearing vibration mode depicted in Figs. 2–6. In the latter case, theoretically, the crack front can be extended (d/a and d/b) in different crack inclination angles (α) by a small amount and the reduction in strain energy of the FGM parallelepiped in a vibratory mode can be calculated. The crack supposedly propagates in such a FGM parallelepiped normal mode of crack opening, shearing, sliding, or tearing in the direction that gives maximum reduction in the strain energy. Analogous albeit not identical evidences are reached by calculating a maximum tensile stress of crack propagation in FGM parallelepiped vibration.

As the crack terminus edge dynamically propagates even a small distance in vibration, the applied stress field in the vicinity of the crack terminus edge no longer satisfies pure crack opening, pure crack shearing or sliding, and pure crack tearing states relative to the crack edge. The resulting FGM parallelepiped vibration modes exhibit mixed opening, shearing, sliding, and tearing stress states relative to the crack edge, as can be seen in Figs. 2–6, depending on the volume fraction ($\hat{m}$), crack length ratios (d/a and d/b), crack positions (c_x/a and c_y/b), and crack inclination angles (α). Under such mixed crack opening, shearing, sliding, and tearing FGM parallelepiped vibratory modes, the crack dynamically propagates in continuously changing direction until settling along a direction perpendicular to the maximum tensile stress state or maximum strain energy release (or reduction) rate. This is what is largely depicted in the 3-D mode shapes corresponding to the nodal pattern contours shown in Figs. 2–6, particularly for the FFFF and CFCF FGM parallelepipeds (Figs. 4–6), where the 3-D modes shapes more clearly depict mixed modes of crack opening, crack shearing or sliding, and crack tearing, more so for FFFF FGM parallelepipeds than CFCF ones, and more so for FGM parallelepipeds having large crack length ratios (d/a and d/b), asymmetric crack positions (c_x/a and c_y/b), and large crack inclination angles (α). As a crack closes potentially causing two sides of the crack to collide with each other during vibration, it is a complicated nonlinear phenomenon of fracture mechanics, which is not considered in the present linear 3-D elasticity-based study—only admissible *crack functions* that properly describe the $\vartheta(1/\sqrt{r})$ 3-D stress singularities at the terminus edge front of the crack, allowing for displacement discontinuities across the crack sufficient to explain the most general 3-D "mixed modes" of local crack-edge deformation and stress fields typically seen in fracture mechanics.

The 3-D mode shapes depicted in Figs. 2–6 show the fully developed deformations of the cracked parallelepiped vibration modes, associated with the nodal patterns also depicted in Figs. 2–6 showing only the deformations on the mid-plane. Blank mode shapes indicate in-plane modes, including predominately crack opening, crack shearing and sliding or crack tearing in some cases. For the out-of-plane flexural modes, the 3-D mode shapes depict the primarily out-of-plane displacements, alongside the nodal patterns showing nodal lines represented by dash lines. As expected, the 3-D mode shapes are not significantly affected by the values of volume fraction ($\hat{m}$).

Depicted in Figs. 2a and 3a are the first five 3-D mode shapes, nodal patterns and $\omega(b^2/h)\sqrt{\rho/E}$ for a SSSS homogeneous (Fig. 2a) and $\omega(b^2/h)\sqrt{\rho_c/E_c}$ for a SSSS Al/Al_2O_3 FGM (Fig. 3a) square parallelepiped modeled as moderately thick plates ($\hat{m}=0$, 5, $d/b=0$, $h/b=0.1$), which show first longitudinal flexure (Mode 1), followed by a pair of second longitudinal flexure showing single nodal lines each transverse to the hinged plate edges (Modes 2 and 3), and finally a pair of longitudinal extension modes, showing in-plane curvatures of parallel hinged plate edges (Modes 4 and 5).

In validation, Fig. 3 compares nodal patterns and $\omega(b^2/h)\sqrt{\rho_c/E_c}$ for SSSS cracked Al/Al_2O_3 FGM square parallelepipeds, modeled as a moderately thick cracked Al/Al_2O_3 FGM plate using third-order Reddy thick plate theory [36] (in Fig. 3c) against the present 3-D elasticity-based theory (in Fig. 3a–b) ($\hat{m}=5$, $d/b=0,0.2,0.5$, $h/b=0.1$, $c_y/b=0.5$, $\alpha=0^\circ$). For the intact SSSS parallelepipeds ($\hat{m}=5, d/b=0$, $h/b=0.1$), the third-order Reddy thick plate theory solutions (listed here in parentheses) slightly under-predicts the correct 3-D solutions for the flexural Mode 1: 3.772 (3.768), Mode 2: 8.927 (8.909), and Mode 3: 8.927 (8.909), yet correctly predicts the 3-D in-plane Mode 4: 12.64 (12.64), and Mode 5: 12.64 (12.64). For the SSSS shallow cracked FGM parallelepipeds ($\hat{m}=5$, $d/b=0.2$, $h/b=0.1$, $c_y/b=0.5$, $\alpha=0^\circ$), the thick plate theory again slightly under-predicts the correct 3-D solutions for the flexural Mode 1: 3.759 (3.756), Mode 2: 8.867 (8.851), Mode 3: 8.885 (8.867), and correctly predicts the 3-D in-plane Mode 4: 12.05 (12.04), and Mode 5: 12.64 (12.64). For the SSSS deep cracked FGM parallelepipeds ($\hat{m}=5$, $d/b=0.5$, $h/b=0.1$, $c_y/b=0.5$, $\alpha=0^\circ$), the thick plate theory again slightly under-predicts the correct 3-D flexural Mode 1: 3.513 (3.511), and Mode 3: 8.635 (8.621), yet significantly over-predicts the correct 3-D flexural Mode 2: 7.334 (7.379), and correctly predicts the 3-D in-plane Mode 4: 10.49 (10.49), and Mode 5: 11.18 (11.17).

In Figs. 2–6, a side crack destroys any modal symmetries about the horizontal or vertical central line of the parallelepipeds, and a shallow crack (i.e., $d/b=0.2$) or a deep side crack (i.e., $d/b=0.5$) does alter the 3-D mode shapes and nodal patterns considerably from those for a correspondingly intact parallelepiped. For instance, an intact SSSS homogeneous parallelepiped modeled as a square thin plate (for $h/a<0.05$), the reference exact values (Leissa, [37]) of the first five $\omega(b^2/h)\sqrt{\rho/E}$ are 5.9737, 14.93, 14.93, 23.89 and 29.87 ($\omega b^2\sqrt{\rho h/D}=n\pi^2$, with $n=2$, 5, 5, 8, 10). For a small cracked ($d/b=0.2$) SSSS parallelepipeds modeled as a moderately thick plates ($h/b=0.1$), it is seen in Fig. 2a–d that a shallow crack (i.e., $d/b=0.2$) causes an unappreciable change in the first three 3-D longitudinal flexure mode shapes and nodal patterns, but the small crack does cause an appreciable change in the $\omega(b^2/h)\sqrt{\rho/E}$ (for homogeneous) and $\omega(b^2/h)\sqrt{\rho_c/E_c}$ (for FGM). As expected, a deep side crack (i.e., $d/b=0.5$) results in decreasing values of $\omega(b^2/h)\sqrt{\rho/E}$ and $\omega(b^2/h)\sqrt{\rho_c/E_c}$ for all modes.

For parallelepipeds with centrally positioned ($c_y/b=0.5$) side cracks, oriented ($\alpha=0^\circ$) parallel to the parallelepiped edges, the free vibration mode shapes are either symmetric or anti-symmetric to one axis ($y=b/2$) of the parallelepiped. This is seen in the nodal patterns (lines of zero displacement) shown in Figs. 2–6. In this case all modes are symmetric (e.g., modes 1, 2, 5)

or anti-symmetric (e.g., modes 3, 4) with respect to that parallelepiped axis, with exceptions of in-plane modes (indicated by an asterisk) which may fall within the first five $\omega(b^2/h)\sqrt{\rho/E}$ and $\omega(b^2/h)\sqrt{\rho_c/E_c}$. For shallow cracked SSSS parallelepipeds ($d/a=0.2$) the node lines seen in Fig. 2 for the first four modes are almost identical to those of the plate with no crack. The difference shows up more clearly for mode 5, where the two diagonal node lines, which are perfectly straight with no crack, are distorted significantly.

Shown in Fig. 4a are the first five 3-D mode shapes, nodal patterns and $\omega(b^2/h)\sqrt{\rho_c/E_c}$ for a FFFF square Al/Al_2O_3 FGM parallelepiped modeled as a moderately thick Al/Al_2O_3 FGM plate ($\hat{m}=5$, $d/b=0$, $h/b=0.1$, $c_x/a=0.5$, $\alpha=0^\circ$), which exhibits as non-rigid body motions, flexure possessing two nodal diameters transverse to the FFFF parallelepiped sides (Mode 1), followed by flexure possessing two nodal diameters emanating from the corners of the FFFF parallelepiped (Mode 2), then flexure characterized by a single nodal circle (Mode 3), and finally a pair of torsional modes featuring a pair of nodal diameters transverse to the parallelepiped sides which are orthogonal to a single nodal diameter transverse to the opposite parallelepiped sides (Modes 4 and 5). Shown in validation in Fig. 4e are reference nodal patterns for a homogeneous intact FFFF parallelepiped ($d/a=0$), showing the first five nonzero $\omega(b^2/h)\sqrt{\rho/E}$ are 4.076, 5.934, 7.348, 10.54 and 10.54 [37,38]. The authors know of no other published frequencies or nodal patterns for FFFF cracked parallelepipeds.

Finally, Fig. 5b shows the first five 3-D mode shapes, nodal patterns and $\omega(b^2/h)\sqrt{\rho/E}$ for CFCF homogeneous cracked rectangular parallelepipeds modeled as moderately thick cracked plates ($\hat{m}=0$, $a/b=2$, $d/b=0.2,0.5$, $h/b=0.1$, $c_x/a=0.5$, $\alpha=90^\circ$), which show evidence of first longitudinal flexure (Mode 1), first torsion featuring a nodal diameter transverse to the parallelepiped sides (Mode 2), second longitudinal flexure including a nodal diameter transverse to the parallelepiped sides (Mode 3), second torsion presenting a pair of orthogonal nodal diameters transverse to the parallelepiped sides (Mode 4), and finally longitudinal extension, showing in-plane curvatures of parallel free edges of the plate, also clearly depicting crack tearing, (Modes 5).

Figs. 2–6 summarize the first five 3-D mode shapes, nodal patterns and $\omega(b^2/h)\sqrt{\rho_c/E_c}$ of SSSS, FFFF, and CFCF rectangular Al/Al_2O_3 and Al/ZrO_2 FGM parallelepipeds with side cracks. The $\omega(b^2/h)\sqrt{\rho_c/E_c}$ displayed in Figs. 2–6 are exact to at least four significant figures. Depicted in Figs. 2–6 are effects of the volume fraction ($\hat{m}=0$, 1, 5, 10), thickness ratios ($h/b=0.02$, 0.1, 0.2, 0.3), crack length ratios (d/a or $d/b=0,1$, 0.2, 0.5), crack positions ($c_y/b=0.5$, 0.75 or $c_x/a=0.25$, 0.5) and crack orientations ($\alpha=0^\circ$, 30°, 45°, 90°, 135°) on the first five 3-D mode shapes and nodal patterns. It should be noted that $\omega(b^2/h)\sqrt{\rho_c/E_c}$ decline as h/b or d/a or d/b increases, as h/b is assumed in the definition of $\omega(b^2/h)\sqrt{\rho_c/E_c}$, and the stiffness of the FGM parallelepipeds decreases with the increase of crack length ratios (d/a or d/b). The frequencies of Al/Al_2O_3 FGM parallelepipeds decrease with the increase of $\hat{m}$, but the trend may not be valid for Al/ZrO_2 FGM parallelepipeds. The $\omega(b^2/h)\sqrt{\rho_c/E_c}$ of CFCF Al/ZrO_2 FGM rectangular parallelepipeds modeled as moderately thick plates ($h/b=0.1$) increase as the volume fraction $\hat{m}=1$ increases to 5, and $\omega(b^2/h)\sqrt{\rho_c/E_c}$ decrease when $\hat{m}=5$ increase further to $\hat{m}=10$.

Across the board in Figs. 2–6 there appears to be no general trends within the first five 3-D mode shapes, nodal patterns and $\omega(b^2/h)\sqrt{\rho_c/E_c}$ of SSSS, FFFF, and CFCF cracked FGM parallelepipeds under the influence of varying with the crack positions and orientations. Nonetheless, the resulting cracked FGM parallelepiped vibration modes in coupled longitudinal flexure, sideways flexure, longitudinal extension, and torsional modes exhibit mixed opening, shearing, sliding, and tearing stress states relative to the crack edge, depending on the volume fraction ($\hat{m}$), crack length ratios (d/a and d/b), crack positions (c_x/a and c_y/b), and crack inclination angles (α). These crack size effects imply flaw-size influence in FGM parallelepiped vibration and fracture, suggesting that these crack size effects can be fully analyzed, only if crack-edge stress singularity analysis (see Appendix), allowing for displacement discontinuities across the crack (sufficient to describe the most general 3-D "mixed-modes" of local crack-edge deformation and stress fields), are conducted, given the dominate ($n=1$) generalized stress intensities, $\sqrt{2\pi}B^{(i)}_{1ml}$ and $\sqrt{2\pi}C^{(i)}_{1ml}$, (predicted by the present 3-D Ritz procedure in Eq. (5) for each cracked FGM parallelepiped normal mode). As the crack is slightly off-set of center (*e.g.*, $c_y/b=0.75$), Figs. 2–6 shows that the frequencies can be either more or less affected by crack offset (c_y/b), depending upon the modes. An off-center crack completely destroys any symmetry, as may be seen in the lack of symmetry in the node lines of Figs. 2–6 (see for example, the SSSS and FFFF parallelepipeds with $\alpha\neq 0^\circ$, $c_y/b=0.75$, and the CFCF parallelepipeds with $\alpha=0^\circ$, $c_y/b=0.25$). For $\alpha\neq 0^\circ$, Figs. 2–6 shows that otherwise symmetrical node lines of intact parallelepipeds are further distorted for cracked FGM parallelepipeds. It is also interesting to note in Figs. 2–6 that node lines may intersect a shallow ($d/b=0.2$) or deep ($d/b=0.5$) crack and, in some cases, even the tip of a crack. One can also contrast in Figs. 2–6 that the presence of an edge crack affects the fundamental (i.e. lowest) frequency of the FFFF cracked FGM parallelepipeds much more than that of the SSSS or CFCF ones. For instance, the fundamental mode shape of an intact FFFF parallelepiped is anti-symmetric, whereas for the SSSS one it is symmetric. But this effect does not extend to the other modes of the parallelepipeds; that is, symmetric mode frequencies in some cases are more greatly affected by a crack than the anti-symmetric modes.

6. Conclusions

Proposed herein is a three-dimensional elasticity-based Ritz procedure to predict accurate vibration frequencies and mode shapes of FGM rectangular parallelepipeds with side cracks. A hybrid set of admissible displacement fields have been proposed, which consists of mathematically complete orthogonal polynomials, and of admissible *crack functions* that properly describe the $\vartheta(1/\sqrt{r})$3-D stress singularities at the terminus edge front of the crack, allowing for displacement discontinuities across the crack sufficient to explain the most general 3-D "mixed modes" of local crack-edge deformation and stress fields typically seen in fracture mechanics. Discussed in this paper is an assessment of the dynamic stress in the vicinity of crack terminus edge, exhibiting in vibration mixed opening, shearing, sliding, and tearing stress states relative to the crack edge.

The efficiency of the proposed admissible functions has been substantiated through comprehensive convergence studies of non-dimensional frequencies for simply-supported, completely free, and clamped-free homogeneous and FGM cracked rectangular parallelepipeds modeled as thin and thick plates with horizontal cracks positioned along a symmetry axis. It is shown that both the hybrid assumed displacement fields of orthogonal polynomials and corner functions indeed accelerate the convergence of numerical solutions, especially for parallelepipeds having a deep (d/a or $d/b=0.5$, see Fig. 1) more than a shallow (d/a or $d/b=0.2$) crack. The convergent results for the cracked thin homogeneous plate ($h/b=0.01$) agree excellently with previously published results based on the classical thin plate theory, confirming the correctness and accuracy of the present 3-D solutions. Convergence studies also demonstrate that the present 3-D approach yields the least upper bounds on the exact solution of cracked homogeneous and FGM rectangular parallelepipeds

modeled as thick plates, when such 3-D solutions are compared against previously published upper bounds on exact solutions using the Ritz method combined with various shear deformable thick plate theories. In addition, the present 3-D approach has been applied to investigate the effects of volume fraction ($\hat{m}$), crack length ratios (d/a and d/b), crack positions (c_x/a and c_y/b), and crack inclination angles (α), on the free vibration frequencies and mode shapes of simply-supported, completely free, and clamped-free parallelepipeds modeled as thick plates with side cracks, including cracks which are not along a symmetry axis, but are skewed. Most of the 3-D results reported are novel, which can be used as standard to judge the accuracy of other numerical methods and various plate theories.

Acknowledgment

This work reported herein was supported by the National Science Council, Taiwan through Research Grant no. NSC98-2221-E-009-075-MY3. Portions of this work was completed while the second author was supported as a National Aeronautics and Space Administration (NASA) Glenn Research Center Summer Faculty Fellow in Brookpark, Ohio USA. Additional support is gratefully acknowledged from the Wright Patterson Air Force Base, Air Force Research Laboratory, Contract no. FA8650-08-D-2806, under technical monitor, Jeffrey Brown (Jeffrey.Brown@wpafb.af.mil) and contract monitor, Joseph Gordon (Joseph.Gordon@wpafb.af.mil).

Appendix: summary of dynamic stress in the vicinity of a FGM parallelepiped crack

Among the acceptable values of $(2n-1)/2$ in the displacement and stress fields (Eqs. (9)–(10)) that yield maximum stresses in the vicinity of the crack terminus edge (Fig. 1) corresponds to $n=1$. As already identified, the crack-edge stress fields are dominated by the order of an inverse square root of a local polar coordinate ($r=\sqrt{x^2+y^2}$, see Fig. 1), $\vartheta(1/\sqrt{r})$, emanating from the crack terminus edge, whereas the crack-edge deformations are dominated by the order of a square root of the local polar coordinate, r, $\vartheta(\sqrt{r})$. For small values of r in the vicinity of the crack terminus edge, the stress fields become extremely large, and the normal mode responses (Figs. 2–6) becomes distorted in free vibration of a cracked FGM parallelepiped having various combinations of clamped, hinged or stress free face conditions. For other integer values of $n=2,3,4,5,\ldots$, the stress fields are bounded yet significantly less at the crack-edge. In summary, near a crack terminus edge, where the terms corresponding to $n=1$ dominates, and given the dominate ($n=1$) generalized stress intensities, $\sqrt{2\pi}B^{(i)}_{1ml}$ and $\sqrt{2\pi}C^{(i)}_{1ml}$, (predicted by the present 3-D Ritz procedure in Eq. (5) for each cracked FGM parallelepiped normal mode), one can determined the dynamic stress fields in the local polar (r,θ) coordinates (see Fig. 1) as follows:

$$\begin{aligned}
&\sigma_x=\lambda(z)(U_{1,r})=\lambda(z)[\hat{U}_{1c,r}],\sigma_\theta=\lambda(z)r^{-1}(U_{2,\theta}+U_1)\\
&\quad=\lambda(z)r^{-1}[\hat{U}_{2c,\theta}+U_{1c}],\\
&\sigma_z=\lambda(z)(U_{3,z})=\lambda(z)[\hat{U}_{3c,z}],\\
&\tau_{r\theta}=\tau_{\theta r}=(G(z)/2)(r^{-1}U_{1,\theta}+U_{2,r}-r^{-1}U_{2,\theta})\\
&\quad=(G(z)/2)[r^{-1}\hat{U}_{1c,\theta}+U_{2c,r}-r^{-1}\hat{U}_{2c,\theta}],\\
&\tau_{\theta z}=\tau_{z\theta}=(G(z)/2)(U_{2,z}+r^{-1}U_{3,\theta})=(G(z)/2)[\hat{U}_{2c,z}+r^{-1}U_{3c,\theta}],\\
&\tau_{rz}=\tau_{zr}=(G(z)/2)(U_{1,z}+U_{3,r})=(G(z)/2)[\hat{U}_{1c,z}+U_{3c,r}].
\end{aligned}\tag{A.1}$$

where $\lambda(z)=\upsilon(z)E(z)/(1+\upsilon(z))(1-2\upsilon(z))$ and $G(z)=E(z)/[2(1+\upsilon(z)]$

$$\hat{U}_{ic}(r,\theta,z)=g_i(r,\theta,z)\sum_{l=1}^{N_{iz}}\sum_{m=0}^{n}\left[B^{(i)}_{1ml}r^{1/2}\cos\left(\frac{2m+1}{2}\theta\right)+C^{(i)}_{1ml}r^{1/2}\sin\left(\frac{2m+1}{2}\theta\right)\right]z^{l-1}\tag{A.2}$$

$$\sigma_r=(\lambda(z)/2)\left\{g_{1,r}(r,\theta,z)\sum_{l=1}^{N_{iz}}\sum_{m=0}^{n}\left[B^{(1)}_{1ml}r^{-1/2}\cos\left(\frac{2m+1}{2}\theta\right)+C^{(1)}_{1ml}r^{-1/2}\sin\left(\frac{2m+1}{2}\theta\right)\right]z^{l-1}\right\}e^{\sqrt{-1}\omega t}\tag{A.3}$$

$$\begin{aligned}
\sigma_\theta=\lambda(z)\Bigg\{&\left(g_{2,\theta}(r,\theta,z)\sum_{l=1}^{N_{2z}}\sum_{m=0}^{n}\left[-\left(\frac{2m+1}{2}\right)B^{(2)}_{1ml}r^{-1/2}\sin\left(\frac{2m+1}{2}\theta\right)+\left(\frac{2m+1}{2}\right)C^{(2)}_{1ml}r^{-1/2}\cos\left(\frac{2m+1}{2}\theta\right)\right]\right.\\
&+g_2(r,\theta,z)\sum_{l=1}^{N_{1z}}\sum_{m=0}^{n}\left[B^{(1)}_{1ml}r^{-1/2}\cos\left(\frac{2m+1}{2}\theta\right)\right.\\
&\left.\left.+C^{(1)}_{1ml}r^{-1/2}\sin\left(\frac{2m+1}{2}\theta\right)\right]\right)z^{l-1}\Bigg\}e^{\sqrt{-1}\omega t}
\end{aligned}\tag{A.4}$$

$$\sigma_z(r,\theta,z)=\lambda(z)\left\{g_{3,z}(r,\theta,z)\sum_{l=1}^{N_{1z}}\sum_{m=0}^{n}\left[B^{(3)}_{1ml}r^{1/2}\cos\left(\frac{2m+1}{2}\theta\right)+C^{(3)}_{1ml}r^{1/2}\sin\left(\frac{2m+1}{2}\theta\right)\right](l-1)z^{l-2}\right\}e^{\sqrt{-1}\omega t}\tag{A.5}$$

$$\begin{aligned}
\tau_{r\theta}=(G(z)/2)\Bigg\{&\left(g_{1,\theta}(r,\theta,z)\sum_{l=1}^{N_{1z}}\sum_{m=0}^{n}\left[-\left(\frac{2m+1}{2}\right)B^{(1)}_{1ml}r^{-1/2}\sin\left(\frac{2m+1}{2}\theta\right)+\left(\frac{2m+1}{2}\right)C^{(1)}_{1ml}r^{-1/2}\cos\left(\frac{2m+1}{2}\theta\right)\right]\right.\\
&+g_{2,r}(r,\theta,z)\sum_{l=1}^{N_{2z}}\sum_{m=0}^{n}\left[B^{(2)}_{1ml}r^{-1/2}\cos\left(\frac{2m+1}{2}\theta\right)\right.\\
&\left.+C^{(2)}_{1ml}r^{-1/2}\sin\left(\frac{2m+1}{2}\theta\right)\right]-g_{2,\theta}(r,\theta,z)\sum_{l=1}^{N_{2z}}\sum_{m=0}^{n}\left[-\left(\frac{2m+1}{2}\right)\right.\\
&\left.\left.B^{(2)}_{1ml}r^{-1/2}\sin\left(\frac{2m+1}{2}\theta\right)+\left(\frac{2m+1}{2}\right)C^{(2)}_{1ml}r^{-1/2}\cos\left(\frac{2m+1}{2}\theta\right)\right]\right)z^{l-1}\Bigg\}e^{\sqrt{-1}\omega t}
\end{aligned}\tag{A.6}$$

$$\begin{aligned}
\tau_{\theta z}=(G(z)/2)\Bigg\{&\left(g_{2,z}(r,\theta,z)\sum_{l=1}^{N_{2z}}\sum_{m=0}^{n}\left[B^{(2)}_{1ml}r^{1/2}\cos\left(\frac{2m+1}{2}\theta\right)+C^{(2)}_{1ml}r^{1/2}\sin\left(\frac{2m+1}{2}\theta\right)\right](l-1)z^{l-2}-g_{3,\theta}(r,\theta,z)\sum_{l=1}^{N_{3z}}\sum_{m=0}^{n}\right.\\
&\left.\left[-\left(\frac{2m+1}{2}\right)B^{(3)}_{1ml}r^{-1/2}\sin\left(\frac{2m+1}{2}\theta\right)+\left(\frac{2m+1}{2}\right)C^{(3)}_{1ml}r^{-1/2}\cos\left(\frac{2m+1}{2}\theta\right)\right]\right)z^{l-1}\Bigg\}e^{\sqrt{-1}\omega t}
\end{aligned}\tag{A.7}$$

$$\begin{aligned}
\tau_{rz}=(G(z)/2)\Bigg\{&\left(g_{1,z}(r,\theta,z)\sum_{l=1}^{N_{1z}}\sum_{m=0}^{n}\left[B^{(1)}_{1ml}r^{1/2}\cos\left(\frac{2m+1}{2}\theta\right)+C^{(1)}_{1ml}r^{1/2}\sin\left(\frac{2m+1}{2}\theta\right)\right](l-1)z^{l-2}-g_{3,r}(r,\theta,z)\sum_{l=1}^{N_{3z}}\sum_{m=0}^{n}\right.\\
&\left.\left[B^{(3)}_{1ml}r^{-1/2}\sin\left(\frac{2m+1}{2}\theta\right)+C^{(3)}_{1ml}r^{-1/2}\cos\left(\frac{2m+1}{2}\theta\right)\right]\right)z^{l-1}\Bigg\}e^{\sqrt{-1}\omega t}
\end{aligned}\tag{A.8}$$

In Eqs. (A.1)–(A.8), it is assumed that the displacement corner functions (A.2) are most dominate ($n=1$) in the local dynamic stress fields in the vicinity of a crack terminus edge of the FGM parallelepiped.

Physically, $\sqrt{2\pi}B^{(i)}_{1ml}$ and $\sqrt{2\pi}C^{(i)}_{1ml}$, may be regarded as the dominant ($n=1$) intensities of vibratory loads through the crack edge region of a FGM parallelepiped. Hence, "mixed mode" cracking in FGM parallelepiped vibration, exhibiting mixed opening, shearing, sliding, and tearing stress states relative to the crack edge, depending on the volume fraction ($\hat{m}$), crack length ratios (d/a and d/b), crack positions (c_x/a and c_y/b), and crack inclination angles (α), is sufficient to describe the most general three-dimensional dynamic "small-scale" yielding of local crack-tip deformation and stress fields in cracked parallelepipeds. Because fracture processes of a functionally graded material may be regarded as "caused" by this surrounding crack-edge stress field nature, the "mixed-mode" intensities $\sqrt{2\pi}B^{(i)}_{1ml}$ and $\sqrt{2\pi}C^{(i)}_{1ml}$ may be interpreted in a generalized sense as fracture correlation coefficients in current practice. It should be noted that these stress intensities have units of (force) $\times$ (length)$^{-3/2}$ [33,34], and since the intensities are linear factors in elastic stress, they must be proportional to the vibratory force, and other characteristic lengths, such as crack size, i.e., determined in the present analysis by various crack length ratios (d/a and d/b), crack positions (c_x/a and c_y/b), and crack inclination angles (α) (see Fig. 1). These crack size effects imply flaw-size influence in FGM parallelepiped vibration and fracture, suggesting that these crack size effects can be fully analyzed only if crack-edge stress singularity effects are incorporated, allowing for displacement discontinuities across the crack (sufficient to describe the most general 3-D "mixed-modes" of local crack-edge deformation and stress fields). For SSSS, FFFF, and CFCF cracked rectangular FGM parallelepiped, the face tractions are determined by the 3-D stress Eqs. (A.3)–(A.8) to maintain dynamic equilibrium of the parallelepiped in the vibratory modes shown in Figs. 2–6. Note that these 3-D stresses are known at all points on the SSSS, FFFF, and CFCF faces.

By assuming simple harmonic motion at peak cycle, $e^{\sqrt{-1}\omega t}\rightarrow 1$, Eqs. (A.1)–(A.8) serve to establish the maximum dynamic fracture stresses from the maximum dynamic energies (Eq. (2)–(3)), first proposed in classical works by Griffith [42]. As determined by crack length ratios (d/a and d/b), crack positions (c_x/a and c_y/b), and crack inclination angles (α) (see Fig. 1), these crack size effects imply original flaw-size area, A, in FGM parallelepiped vibration and fracture, in which such flaw-size area may be ideally propagated, as $A+\Delta A$ during vibration in mixed opening, shearing, sliding, and tearing stress states relative to the crack edge (see Figs. 2–6). When the maximum dynamic energies (Eq. (2)–(3)), induced by progressing from a cracked FGM parallelepiped vibratory state to another one wherein the crack is slightly propagated during vibration, is greater than the maximum dynamic energies of a cracked-propagated FGM parallelepiped vibratory state, then the cracked FGM parallelepiped vibrates from an non-propagated (n–p) to a propagated (p) state, because the parallelepiped achieves a minimum dynamic energy, according to the Griffith theory [42].

In using the present Ritz procedure, the maximum dynamic characteristics of the cracked parallelepiped vibrating from a non-propagated to a propagated flaw-size state may be predicted by the energy functional:

$$\begin{aligned} &\Pi_{n-p} = (V_{\max} - T_{\max})_{n-p} \\ &\Pi_{p} = (V_{\max} - T_{\max})_{p} \end{aligned} \tag{A.9}$$

where $V_{\max}$ is the maximum strain energy (Eq. (3a)), and $T_{\max}$ is the maximum kinetic energy (Eq. (3b)) in simple harmonic motion, $e^{\sqrt{-1}\omega t}\rightarrow 1$, at peak crack displacements and crack stresses (Eqs. (A.1)–(A.8)) of the vibratory cycle. Neglected herein are any generations in heat energy in the FGM parallelepiped due to temperature gradients associated with vibratory crack propagation, or any plastic dissipation associated with such dynamic crack broadening. Thus, the Griffith's criterion for such potential crack propagation during FGM parallelepiped vibration is (π_c being the surface energy per unit area of new flaw-size surface, ΔA):

$$\begin{aligned} &\Pi_{n-p} \geq \Pi_p + \int_{\Delta A} \pi_c dA \\ &\Rightarrow \Pi_p - \Pi_{n-p} + \textstyle\int_{\Delta A} \pi_c dA \leq 0 \end{aligned} \tag{A.10}$$

For $\Delta A \rightarrow 0$,

$$\begin{aligned} &\Rightarrow \tfrac{\Pi_p - \Pi_{n-p}}{\Delta A} + \pi_c \leq 0 \\ &\Rightarrow \tfrac{\Delta \Pi}{\Delta A} + \pi_c \leq 0 \end{aligned} \tag{A.11}$$

Hence, as $\Delta A \rightarrow 0$, according to Griffith [42], as $\frac{\Delta \Pi}{\Delta A} + \pi_c \leq 0$, the crack propagates and the FGM parallelepiped vibrates from an non-propagated to a propagated flaw-size state. In contrast, as $\frac{\Delta \Pi}{\Delta A} + \pi_c > 0$, the FGM parallelepiped does not vibrate to a propagated state, largely because the cracked FGM parallelepiped is vibrating at lower energy in a non-propagated flaw-size state and hence more stable energy than in a propagated flaw-size state.

References

[1] Niino M, Maeda S. Recent development status of functionally gradient materials. ISIJ Int. 1990;30:699–703.
[2] Huang CS, Leissa AW. Vibration analysis of rectangular plates with side cracks via the Ritz method. J Sound Vibr 2009;323(3-5):974–88.
[3] Huang CS, Leissa AW, Liao SC. Vibration analysis of rectangular plates with edge V-notches. Int J Mech Sci 2008;50:1255–62.
[4] Li RS. Vibrations of rectangular cracked Mindlin plates via the Ritz method. MS thesis. Taiwan: National Chiao Tung University; 2009.
[5] Huang CS, Chang MJ. Geometrically induced stress singularities of a thick FGM plate based on the third-order shear deformation theory. Mech Adv Mater Struct 2009;16(2):83–97.
[6] Lynn PP, Kumbasar N. Free vibrations of thin rectangular plates having narrow cracks with simply supported edges. Developments in Mechanics. In: Proceedings of the 10th midwestern mechanics conference, vol. 4. Fort Collins, Colorado: Colorado State University; August 21–23, 1967. p. 911–28.
[7] Stahl B, Keer LM. Vibration and stability of cracked rectangular plates. Int J Solids Struct 1972;8(1):69–91.
[8] Aggarwala BD, Ariel PD. Vibration and bending of a cracked plate. Rozpr Inz 1981;29(2):295–310.
[9] Neku K. Free vibration of a simply-supported rectangular plate with a straight through-notch. Bull Jpn Soc Mech Eng 1982;25(199):16–23.
[10] Solecki R. Bending vibration of a simply supported rectangular plate with a crack parallel to one edge. Eng Fract Mech 1983;18(6):1111–8.
[11] Hirano Y, Okazaki K. Vibration of cracked rectangular plates. Bull Jpn Soc Mech Eng 1980;23(179):732–40.
[12] Qian GL, Gu SN, Jiang JS. A finite element model of cracked plates and application to vibration problems. Comput Struct 1991;39(5):483–7.
[13] Krawczuk M. Natural vibrations of rectangular plates with a through crack. Arch Appl Mech 1993;63(7):491–504.
[14] Yuan J, Dickinson SM. The flexural vibration of rectangular plate systems approached by using artificial springs in the Rayleigh–Ritz method. J Sound Vibr 1992;159(1):39–55.
[15] Liew KM, Hung KC, Lim MK. A solution method for analysis of cracked plates under vibration. Eng Fract Mech 1994;48(3):393–404.
[16] Lee HP, Lim SP. Vibration of cracked rectangular plates including transverse shear deformation and rotary inertia. Comput Struct 1993;49(4):715–8.
[17] Maruyama K, Ichinomiya O. Experimental study of free vibration of clamped rectangular plates with straight narrow slits. JSME Int J Ser III 1989;32(2):187–93.
[18] Ma CC, Hsieh DM. Full-field experimental investigations on resonant vibration of cracked rectangular cantilever plates. AIAA J 2001;39(12):2419–22.
[19] Ma CC, Huang CH. Experimental and numerical analysis of vibrating cracked plates at resonant frequencies. Exp Mech 2001;41(1):8–18.
[20] Yang Y, Shen HS. Dynamic response of initially stressed functional graded rectangular thin plates. Compos Struct 2001;54:497–508.
[21] He XQ, Ng TY, Sivashanker S, Liew KM. Active control of FGM plates with integrated piezoelectric sensors and actuators. Int J Solids Struct 2001;38:1641–55.
[22] Zhao X, Lee YY, Liew KM. Free vibration analysis of functionally graded plates using the element-free kp-Ritz method. J Sound Vibr 2009;319:918–39.
[23] Reddy JN. Analysis of functionally graded plates. Int J Numer Method Eng 2000;47(1-3):663–84.
[24] Matsunaga H. Free vibration and stability of functionally graded plates according to a 2-D higher-order deformation theory. Compos Struct 2008;82:499–512.
[25] Qian LF, Batra RC, Chen LM. Static and dynamic deformations of thick functionally graded elastic plates by using higher-order shear and normal

deformable plate theory and meshless local Petrov–Galerkin method. Compos: Part B 2004;35:685–97.
[26] Vel SS, Batra RC. Three-dimensional exact solution for the vibration of functionally graded rectangular plates. J Sound Vibr 2004;272(3):703–30.
[27] Reddy JN, Cheng ZQ. Frequency of functionally graded plates with three-dimensional asymptotic approach. J Eng Mech ASCE 2003;129(8):896–900.
[28] Bhat RB. Natural frequencies of rectangular plates using characteristic orthogonal polynomials in Rayleigh–Ritz method. J Sound Vibr 1985;102(4):493–499.
[29] Hartranft RJ, Sih GC. The use of eigenfunction expansions in the general solution of three-dimensional crack problems. J Math Mech 1969;19(2):123–138.
[30] Chaudhuri RA, Xie M. A novel eigenfunction expansion solution for three-dimensional crack problems. Compos Sci Technol 2000;60:2565–80.
[31] Williams ML. Surface stress singularities resulting from various boundary conditions in angular corners of plates under bending. In: Proceedings of the first U.S. national congress of applied mechanics. p. 325–9.;
Idem. Stress distribution at the base of a stationary crack. ASME J Appl Mech 1957;24:109–14;
Idem. The bending stress distribution at the base of a stationary crack. ASME J Appl Mech 1961;28:78–82.
[32] Erdogan F, Sih GC. On the crack extension in plates under plane loading and transverse shear. ASME J Basic Eng 1963;85D:519.
[33] Irwin GR. Analysis of stresses and strains near the end of a crack transversing a plate. ASME J Appl Mech 1957;24:361.
[34] Westergaard HM. Bearing pressures and cracks. ASME J Appl Mech 1939;66:49.
[35] Huang CS, Chang MJ. Corner stress singularities in a FGM thin plate. Int J Solids Struct 2007;44(9):2802–19.
[36] Huang CS, McGee III OG, Chang MJ. Vibrations of cracked rectangular FGM thick plates. Compos Struct 2011;93:1747–64.
[37] Leissa AW. Vibration of plates. NASA SP-160 1969. Reprinted 1993 by the Acoustical Society of America.
[38] Filipich CP, Rosales MB. Arbitrary precision frequencies of a free rectangular thin plate. J Sound Vibr 2000;230(3):521–39.
[39] Khadem SE, Rezaee M. Introduction of modified comparison functions for vibration analysis of a rectangular cracked plate. J Sound Vibr 2000;236(2):245–58.
[40] Kim JW, Jung HY. Influence of stress singularities on the vibration of rhombic plates with V-notches or sharp cracks. Key Eng Mater 2004;270-273:1414–9.
[41] Leissa AW, McGee OG, Huang CS. Vibrations of circular plates having V-notches or sharp radial cracks. J Sound Vibr 1993;161(2):227–39.
[42] Griffith AA. The phenomena of rupture and flow in solids. Philos Trans R Soc Lon 1921;A221:163–98;
Idem. The theory of rupture. In: Biezenno CB, Burgers JM, editors. Proceedings of the first international congress of applied mechanics. Delft: Waltman; 1924. p. 55–63.